Inorganic Chemistry

pubs.acs.org/IC Article

Magnetic Anisotropy in the Homoleptic $[CoX_4]^{2-}$ (X = Cl, Br, I) Series: Spectroscopic Determination and Ligand Field Studies

Adiat A. Fakolujo, Michael J. Jenkins, J. Krzystek, You Song, Xiaoping Wang, Yongqiang Cheng, Luke L. Daemen, Mykhaylo Ozerov, Joshua Telser, Zhao-Bo Hu, and Zi-Ling Xue*

Cite This: *Inorg. Chem.* 2026, 65, 12818−12834 Read Online

ACCESS | Metrics & More | Article Recommendations | Supporting Information

ABSTRACT: Four-coordinate transition metal complexes with unpaired electrons ($S \geq 1$) typically exhibit structures deviated from perfect T_d geometry, leading to magnetic anisotropy. $(NEt_4)_2[CoX_4]$ (X = Cl, **Co−Cl**; Br, **Co−Br**; I, **Co−I**) with pseudotetrahedral structures are an ideal series to explore how deviation from perfect T_d geometry is reflected in magnetic anisotropy. This work presents comprehensive studies of **Co-X**, including single-crystal X-ray diffraction of **Co−Cl** and **Co−I**, measurements of DC and AC magnetic susceptibilities, inelastic neutron scattering (INS), far-infrared magneto-spectroscopy (FIRMS), and high-frequency and -field electron paramagnetic resonance (HFEPR). Both $[CoCl_4]^{2-}$ and $[CoBr_4]^{2-}$ ions have crystallographically imposed D_{2d} symmetry, while the $[CoI_4]^{2-}$ ion adopts slightly distorted tetrahedral geometry approximating D_{2d} symmetry. Magnetic anisotropy increases from **Co−Cl** to **Co−I**. Also, only **Co−Cl** and **Co−Br** show field-induced SMM behaviors. FIRMS of **Co−I** reveals spin-phonon couplings, suggesting that these couplings may lead to fast magnetic relaxation and the lack of SMM behavior. Ligand field theory calculations indicate that an increase in spin-orbit couplings (SOC) from **Co−Cl** to **Co−Br** and to **Co−I** leads to increased magnetic anisotropy. These compounds provide insight into how crystal fields, crystallographic symmetries, and SOC affect magnetic anisotropy and spin relaxation in a well-defined series of homoleptic complexes.

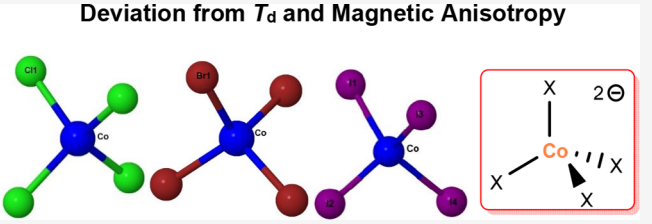

INTRODUCTION

Single-molecule magnets (SMMs) have been proposed as a new generation of data storage materials and for qubit applications, because SMMs are magnetically bistable with spin reversal barriers (U).[1−17] For many complexes, zero-field splitting (ZFS) parameters D and E govern magnetic anisotropy with the simplified spin Hamiltonian inside applied magnetic fields (eq 1):

$$\hat{H}_S = D\left(\hat{S}_z^2 - \frac{1}{3}S(S+1)\right) + E(\hat{S}_x^2 - \hat{S}_y^2) + \mu_B g_x B_x S_x + \mu_B g_y B_y \hat{S}_y + \mu_B g_z B_z \hat{S}_z \quad (1)$$

where $\hat{S}_z$, $\hat{S}_y$, $\hat{S}_x$ = spin operators in the x, y, and z directions; μ_B = electron Bohr magneton; g_x, g_y, g_z = g-factor components; $\boldsymbol{B}$ = ($\boldsymbol{B}_x$, $\boldsymbol{B}_y$, $\boldsymbol{B}_z$), applied magnetic field vector. D, E, g_x, g_y, g_z are called spin-Hamiltonian parameters.

ZFS refers to the splitting of the spin microstate degeneracy in $S \geq 1$ compounds in the absence of an applied field. The $2S + 1$ (= 4 for high-spin Co^{2+} complexes, $3d^7$, $S = 3/2$) degeneracy is lifted in such systems mainly due to lowered molecular symmetry from cubic: octahedral O_h or tetrahedral T_d.[17,18] The degeneracy is removed when the ligand along the z-axis is different from those in the x, y directions, producing Kramers doublets (KDs) in compounds with odd numbers of unpaired electrons as a result of second-order spin-orbit coupling (SOC).[18]

If $D > 0$, magnetization of the compound occurs along the x,y plane, and the anisotropy is called easy-plane. If $D < 0$, magnetization is along the z axis, and the anisotropy is called easy-axis. For the former, quantum tunneling occurs more readily than for the latter, because the transitions within the ground KD ($M_S = \pm 1/2$) is allowed.[19,20] Transverse or rhombic parameter E shows anisotropy between the x and y axes and manifests when the crystallographic symmetry of the metal site is lower than 3-fold ($x \neq y \neq z$). This further splits the KD, and consequently, mixes KDs,[21] leading to faster relaxation, which is typically not desirable in SMMs. Magnetic anisotropies in several types of materials have been studied.[15,22−36]

High-spin ($S = 3/2$) Co^{2+} is a commonly investigated ion for SMM applications.[10,37−39] In tetrahedral Co^{2+} complexes, the ground electronic ^4F state of the free Co^{2+} ion is split into $^4A_2$,

Received: January 22, 2026
Revised: May 5, 2026
Accepted: May 11, 2026
Published: June 4, 2026

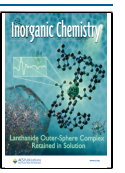

https://doi.org/10.1021/acs.inorgchem.6c00405
Inorg. Chem. 2026, 65, 12818−12834

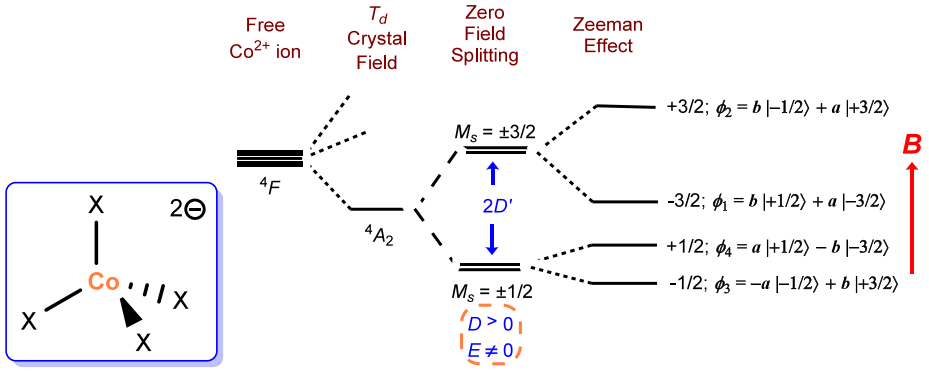

Figure 1. ZFS splitting energy diagram for tetrahedral Co^{2+} complexes with $D > 0$ and $E \neq 0$. $a = \cos\beta$ and $b = \sin\beta$ are mixing coefficients described by the mixing angle β that depends on the rhombicity as $\tan 2\beta = \sqrt{3}\,(E/D)$.[26]

$^4T_2$, and $^4T_1$, with the $^4A_2$ as the ground state (Figure 1).[40] This $^4A_2$ ground state serves as an ideal system for examining how deviations from perfect tetrahedral geometry influence magnetic anisotropy, owing to quenched orbital angular momentum of this state. In comparison, five and six-coordinate Co^{2+} complexes may have an appreciable orbital contribution to their magnetic anisotropy, giving large magnetic anisotropy (e.g., hundreds of cm^{-1}) and substantial g anisotropy. In tetrahedral complexes, D-values are typically small, and g-values are relatively isotropic (larger than 2.0),[18] because of the second-order SOC.

$[Co(SPh)_4]^{2-}$ with an easy-axis anisotropy ($D = -70\ cm^{-1}$) reported by Long and co-workers[41] demonstrates slow relaxation without an applied field. Several pseudotetrahedral Co^{2+} complexes show slow magnetic relaxation under applied fields with field-induced SMM behaviors.[23,42−45] Dunbar and co-workers studied ligand effects on axial ZFS parameters of $Co(quinolone)_2I_2$ and $Co(EPh_3)_2I_2$ (E = P, As),[34] showing an increase in D for those with heavier donor atoms, particularly between P and As.[46] Some of us have studied $Co(PPh_3)_2X_2$ (X = Cl, Br, I) (C_{2v})[33] and $Co(AsPh_3)_2I_2$ (C_{2v}) by both far-infrared magneto-spectroscopy (FIRMS) and inelastic neutron scattering (INS), observing transitions between KDs and determining spin-Hamiltonian parameters for the complexes. $(NEt_4)[Co(PPh_3)X_3]$ (X = Cl, Br) (C_{3v}) has also been studied by DC and AC magnetometry and high-frequency and -field electron paramagnetic resonance (HFEPR) to determine their spin-Hamiltonian parameters.[47] These tetracoordinate Co(II) complexes, except $[Co(SPh)_4]^{2-}$, are all heteroleptic with pnictogen (group 15) and halide (group 17) ligands. We focus here on simpler, homoleptic halide complexes $[CoX_4]^{2-}$ (X = Cl, Br, I) to explore how the degree of deviation from perfect T_d geometry leads to magnetic anisotropy. Characterization techniques such as UV-visible and IR spectra, phase changes, and crystal structures in complexes with the $[CoX_4]^{2-}$ anions but different cations, including the current NEt_4^+, have long been reported.[48−72] Magnetic anisotropies have also been probed in several $[CoX_4]^{2-}$ with different cations.[73−77] Gerloch and co-workers in 1972 measured single-crystal magnetic susceptibility of **Co−Cl** and **Co−Br** and predicted their ZFS values,[61] showing that the magnetic anisotropy is mostly affected by the distortion of the X-Co-X bond angles from perfect tetrahedral geometry and SOC. Styczeń and co-workers have reported the crystal structure of **Co−Br** at room temperature and its DC magnetic susceptibility and EPR properties.[78] These results showed that there are no unusual short-range intermolecular interactions in the crystal lattice, and the fitting of the magnetic susceptibility data showed a negative zJ value of $-0.22\ cm^{-1}$ (zJ = intermolecular interaction parameter), indicative of weak antiferromagnetic interactions within the lattice. Their fit of the DC susceptibility gave $D = +4.11\ cm^{-1}$. In addition, crystal structures of **Co−Cl** (with no cif file),[79] **Co−Br** at room temperature,[78,80] and **Co−I** at 100 K[81] have been reported, all showing disorders of the NEt_4^+ cations. Despite all this prior work, the nature of magnetic anisotropy in $(NEt_4)_2[CoX_4]$ complexes and their potential as SMMs are still not clear. These homoleptic **Co-X** complexes ($[CoX_4]^{2-}$, X = Cl, Br, I), which lack the complication of Jahn−Teller distortions, can provide insight into how crystal field, SOC, crystallographic point group symmetry, and crystal packing forces influence magnetic anisotropy and spin-lattice relaxation.

ZFS parameters are commonly estimated by fitting DC magnetic susceptibility data. However, this method is indirect and susceptible to significant errors. More precise determination of ZFS parameters can be achieved through advanced spectroscopic techniques, such as HFEPR, FIRMS, INS, and, less often, Raman magneto-spectroscopy (RaMS).[23,26,30,82−84]

In this study, we have investigated the magnetic anisotropy and relaxation mechanisms of $(NEt_4)_2[CoX_4]$ complexes (X = Cl, **Co−Cl**; Br, **Co−Br**; I, **Co−I**) using advanced spectroscopic techniques, including HFEPR, FIRMS, INS, and SQUID magnetometry, both direct current (DC) and alternating current (AC) measurements. Additionally, single-crystal X-ray structures were determined for **Co−Cl** and **Co−I** at 100 K and for **Co−Br** at 295 K. Ab initio ligand field theory calculations (AILFT) and ligand field theory (LFT) calculations have been performed to elucidate the origin of the observed magnetic anisotropy. This work examines the tetrahedral complexes that deviate slightly from the ideal T_d symmetry, each with local D_{2d} symmetry but crystallizing in different space groups, to elucidate how packing and symmetry govern magnetic anisotropy and relaxation, supported by advanced spectroscopic techniques that yield accurate transition energies and spin-relaxation parameters.

RESULTS AND DISCUSSION

Crystal Structures and *SHAPE* Analysis

Single-crystal structures of **Co−Cl**, **Co−I** at 100(2) K, and **Co−Br** at 295(2) K have been determined in the current work. Two independent crystal structures of **Co−Br** at room temperature were reported in 2010.[78,80] We obtained a

https://doi.org/10.1021/acs.inorgchem.6c00405
Inorg. Chem. 2026, 65, 12818−12834

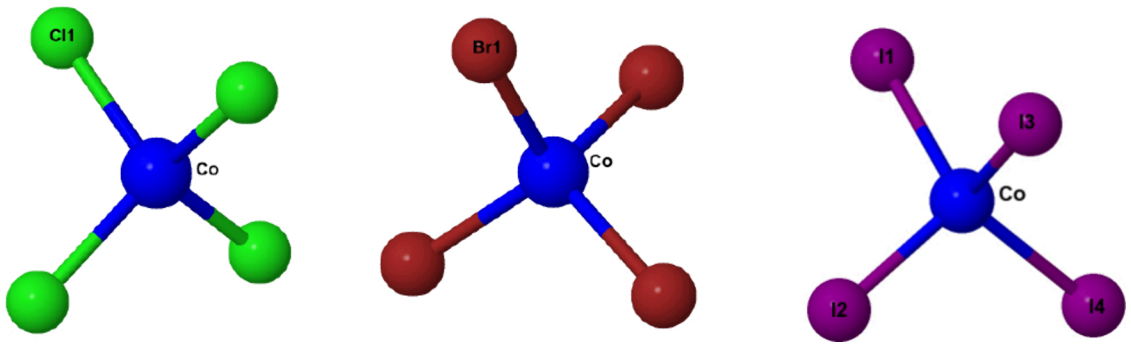

Figure 2. Anion structures of **Co−Cl** reported **Co−Br**, and **Co−I.** Blue, green, brown, and purple represent Co, Cl, Br, and I atoms, respectively. All four chlorides in **Co−Cl** and bromides in **Co−Br** are crystallographically equivalent.

Table 1. Crystal Data for Co−Cl, Co−Br, Co−I, and the Reported Co−Br

compound	**Co−Cl**	**Co−Br** (reported)[a]	**Co−Br** (current)[b]	**Co−I**
space group	tetragonal, $P4_2/nmc$ (No. 137)	tetragonal, $P4_2/nmc$ (No. 137)	tetragonal, $P\text{-}42_1c$ (No. 114)	orthorhombic, $P2_12_12$ (No. 18)
temperature (K)	100(2)	295(2)	295(2)	100(2)
a (Å)	8.7426(3)	8.9856(6)	8.9864(13)	13.633(3)
b (Å)	8.7426(3)	8.9856(6)	8.9864(13)	13.683(3)
c (Å)	15.2212(6)	16.0006(8)	15.955(3)	14.800(3)
Co−X bond lengths (Å)	2.2771(14)	2.4007(9)	2.3957(8)	2.4165(8)−2.7857(10) (average: 2.6191 Å)
range of X−Co−X bond angles (°)	100.82(17)−113.96(9)	108.49(6)−109.97(3)	108.75(5)−109.83(3)	106.38(4)−114.32(3)
shortest Co−Co distance (Å)	9.805	10.216	8.9864	10.056
SHAPE analysis (CShM)	0.710	0.005	0.004	0.459

[a]Crystal structure of **Co−Br** at room temperature was reported in ref 80 [295(2) K] and ref 78 [293(2) K]. The former structure with a lower *R*-factor is cited here. [b]Current work.

different **Co−Br** structure with a lower residual error (R = 4.76%) compared to the reported (6.73[80] and 7.03%[78]). We also collected single-crystal X-ray diffraction data of **Co−Br** at 100 K, but the structure at this low temperature was too disordered to be solved. We also collected single-crystal X-ray diffraction data of **Co−Cl** and **Co−I** at 295(2) K, but they were also too disordered to be solved. The crystal structures of **Co-X**, including a reported **Co−Br** (with R = 6.73%),[80] are summarized and compared in Figure 2 and Table 1, including selected bond angles and lengths for **Co-X**.

Both **Co−Cl** at 100(2) K and **Co−Br** at 295(2) K crystallize in the tetragonal space group $P4_2/nmc$ (No. 137) with one unique molecule in the unit cell. The crystal of **Co−I** is in the orthorhombic $P2_12_12$ space group with one unique molecule in the unit cell. Although the $[CoCl_4]^{2-}$ anion in **Co−Cl** is disordered, both $[CoX_4]^{2-}$ (X = Cl, Br) anions are in tetragonally compressed D_{2d} symmetry. All four Co−Cl bond lengths are equal at 2.2771(14) Å. Among the six Cl−Co−Cl bond angles, four are at 113.96(9)° and the other two are at 100.82(17)°. Similarly, in the $[CoBr_4]^{2-}$ structure in **Co−Br**, lengths of the four Co−Br bonds are at 2.3957(8) and 0.1186 Å longer than the Co−Cl bond. Four of the Br−Co−Br bond angles are at 109.83(3)°, while the remaining two angles are at 108.75(5)°. The orthorhombic $P2_12_12$ (No. 18) space group in **Co−I** makes the four Co−I bond lengths different [2.4165(8) Å, 2.6083(9) Å, 2.6657(11) Å, and 2.7857(10) Å; Average = 2.6191 Å]. In other words, the $[CoI_4]^{2-}$ anion is in the C_1 point group with no symmetry. The average Co−I bond length of 2.6191 Å is 0.2234 and 0.3420 Å longer than those of Co−Br and Co−Cl bonds, respectively. The six I−Co−I bond angles are different from each other in the 106.38(4)°−114.32(3)° range with average of 109.43°. The above-described crystal structures (Figure 2) provide metrics that can be used for ligand field theory, specifically the angular overlap model (AOM).[72,85] For the AOM, we define in each complex four ligands at idealized ϕ values of 0, 90, 180, and 270°. The variation is in their θ values, which are 58.79° (121.21°) for **Co−Cl**, 59.50° (120.50°) for **Co−Br**, and 57.88° (122.12°) for **Co−I**. This last case represents an idealized D_{2d} situation for **Co−I** so that all three complexes are treated equivalently by the AOM. These θ values represent an axial compression from the ideal tetrahedral (T_d) situation with z defined along the S_4 axis of θ = 54.74° (125.26°).

SHAPE analyses of **Co−Cl** and **Co−I** at 100(2) K and **Co−Br** at 293(2) K reveal the degrees to which the three structures are deviated from the perfect tetrahedron, giving *Continuous Shapes Measure* (*CShM*) values of 0.710, 0.005, and 0.459, respectively. Note that the value of **Co−Br** is very small compared to those of **Co−Cl** or **Co−I**. However, the **Co−Br** structure, giving its small *CShM* value, was determined at 293(2) K, while **Co−Cl** and **Co−I** structures were obtained at 100(2) K. At 293(2) K, the **Co−Br** structure is more equalized to ideal T_d. These structure-temperature correlations are consistent with previous studies.[86,87] Specifically, Nover and Schmidtke extensively investigated tetrahedral complexes, including $(NEt_4)_2[CoX_4]$ (**Co-X**), and found from a single-crystal optical spectroscopic measurement at 2 K that the anion is more distorted from tetrahedral geometry than at room temperature.[86] Far-IR spectra of a **Co−Cl** single crystal at room temperature and 105 K by Dunsmuir and Lane

https://doi.org/10.1021/acs.inorgchem.6c00405
Inorg. Chem. 2026, 65, 12818−12834

showed changes in the lattice vibrations owing to distortion from tetrahedral geometry.[87]

Magnetic Susceptibility Studies

Direct-current (DC) susceptibility measurements of the compounds were taken at 0.1 T applied magnetic field in the range of 1.8−300 K. These complexes are paramagnetic, giving values of $\chi_M T$ at room temperature of 2.56 (**Co−Cl**), 2.63 (**Co−Br**), and 2.70 (**Co−I**) $cm^3\ mol^{-1}\ K$ which are larger than the calculated spin-only value ($\chi_M T$ = 1.87 $cm^3\ mol^{-1}$ K, 3.87 μ_B for S = 3/2 with g = 2.0), but they are consistent with reported values for tetrahedral Co(II) complexes with orbital contributions to the magnetic moment.[88,89] The $\chi_M T$ plots (Figure 3) gradually decrease with temperature due to ZFS[90]

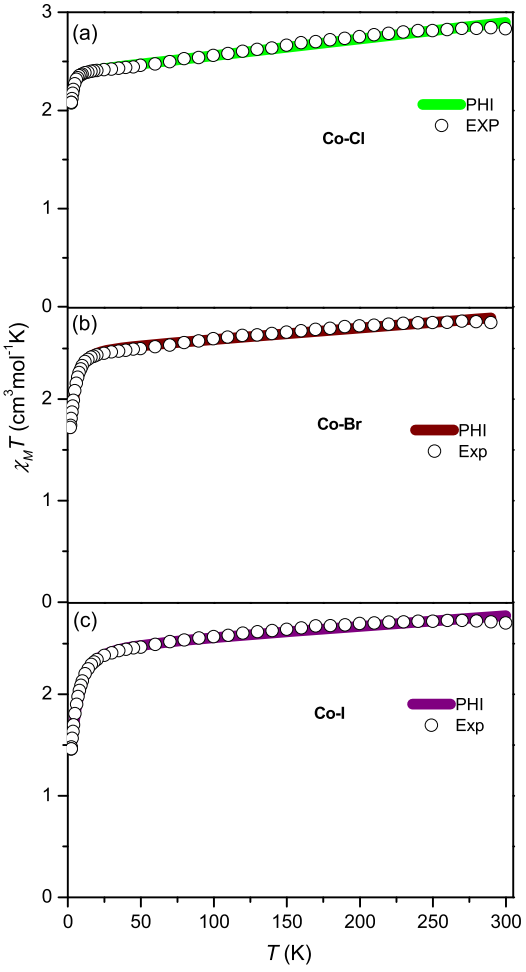

Figure 3. DC magnetic susceptibilities: (a) **Co−Cl**; (b) **Co−Br**; (c) **Co−I**. Fit lines use the parameters given in Table 2.

and reach the smallest value at about 1.8 K, the lowest temperature possible in the magnetometer, in the three complexes. Fitting of the DC data using the *PHI* program yielded D, E, and g values listed in Table 2 with additional details such as zJ and TIP (temperature-independent paramagnetism) data given in Table S2 in SI.[91,92] For **Co−Cl** and **Co−I**, both D values are positive and increase from +2.3(3) cm^{-1} for **Co−Cl** to +7.5(1) cm^{-1} for **Co−I**, indicating that these two complexes have easy-plane magnetic anisotropy. The results are consistent with those from HFEPR discussed below. For **Co−Br**, even though the fitting of the DC data gives D = +4.7(4) cm^{-1}, $|E|$ = 1.3(3) cm^{-1} and $|E/D|$ = 0.28(9), HFEPR gives D = 4.515(10) cm^{-1}, $|E|$ = 1.505(10) cm^{-1} and $|E/D|$ = 0.333(3). Since $|E/D|$ = 1/3 (maximally rhombic) for **Co−Br**, the simple easy-axis vs easy-plane classification is no longer appropriate. The $2D'$ [= $2(D^2 + 3E^2)^{1/2}$] values from the DC data fittings are 4.8(8) cm^{-1} for **Co−Cl**, 10.4(7) cm^{-1} for **Co−Br**, and 15.0(1) cm^{-1} for **Co−I**.

Determination of Spin-Hamiltonian Parameters by HFEPR

HFEPR has been used extensively to probe molecular magnetism,[17,33,34,47,93−104] including determining ZFS. The approximate energy range of HFEPR for this determination is ≤33 cm^{-1} in non-Kramers (S = integers) and ≤15 cm^{-1} in Kramers (S = half integers) complexes with the magnetic field of up to 16 T for the facilities at the US National High Magnetic Field Laboratory (NHMFL).

HFEPR spectra of these compounds were obtained using the EMR facility at NHMFL. Simulations of the spectra using spin-Hamiltonian parameters in Table 2 reveal good fits to the experimental spectra. Complex **Co−Cl** (Figure 4a) measured at 4.5 K and 148 GHz shows a near-ZFS frequency of the inter-Kramers transition between the two lowest Kramers doublets, which immediately yields the approximate $2D'$ value. This frequency corresponds to an energy of 4.9 cm^{-1}. Complex **Co−Br** (Figure 4b) also gave an excellent EPR response at 4.5 K and 310 GHz, which exactly corresponds to the frequency of the ZFS transition between the two lowest Kramers doublets. This frequency corresponds to an energy of 10.3 cm^{-1}, which immediately yields the approximate $2D'$ value. There is a maximum E value of 1.505(10) cm^{-1} [$|E/D|$ = 0.333(3)] for **Co−Br**, even though its crystal structure at 295(2) K is in a tetragonal space group with D_{2d} point group symmetry (with 2-fold degeneracy $x = y$). Since HFEPR was taken at 4.5 K, we believe there is a phase change(s) between room temperature and the liquid helium temperature, leading to significant deviations from the D_{2d} symmetry and giving the rhombic ZFS parameter observed by HFEPR at 4.5 K. Serious distortion of the **Co−Br** structure at 100(2) K from our single-crystal X-ray diffraction data, which we could not solve, supports this view.

The EPR response of **Co−I** was much weaker in terms of signal amplitude than those of its two congeners described above (Figure 4c). This is due to the extremely broad line width of the turning points, about an order of magnitude larger than those of the **Co−Cl** and **Co−Br** compounds. As a result, we were only able to register spectra at a few of the available frequency harmonics, specifically those that produced the most sub-THz wave power. For that reason, no field vs frequency maps could be constructed, and the SH parameters are only estimates obtained from single-frequency spectra. The fitting of single-frequency spectra of all the compounds showed positive D values.

No conventional (e.g., X-band) EPR spectra were recorded for any of the three **Co-X** complexes, given the availability of HFEPR and FIRMS. But effective g' values (i.e., S' = 1/2) were calculated using perturbation theory equations[105] and are given in Table S7. Simulated X-band (9.5 GHz, 77 K) EPR spectra are shown in Figure S16. The difference in spectral appearance between **Co−Cl** and **Co−Br** with perfectly rhombic ZFS and **Co−I** with essentially axial ZFS is readily apparent.

INS Studies

In INS spectroscopy, the sample is bombarded with incident neutrons, leading to magnetic and phonon excitations.[30,94,106−120] Phonons here refer to both external

https://doi.org/10.1021/acs.inorgchem.6c00405
Inorg. Chem. 2026, 65, 12818−12834

Table 2. Spin-Hamiltonian Parameters of Co-X Determined by Different Methods Including Ab Initio Ligand Field Theory (AILFT) and Ligand Field Theory (LFT) Calculations

	method	D (cm^{-1})	$\|E\|$ (cm^{-1})	$\|E/D\|$	$2D'$ (cm^{-1})	g	g_x, g_y, g_z
Co−Cl[a]	DC susceptibility	+2.3(3)	0.4(5)	0.2(2)	4.8(8)	2.257(1)	
	HFEPR	+2.48(1)	0.0840(10)	0.0339(5)	4.96(1)		2.32(1), 2.34(1), 2.309(5)
	LFT				4.98,[b] 4.97[c]		
$[CoCl_4]^{2-}$ without cations[d]	AILFT-CASSCF	+26.58		0.099			2.255, 2.557, 2.617
	AILFT-NEVPT2	+20.44		0.106			2.206, 2.431, 2.482
Co−Br	DC susceptibility	+4.7(4)	1.3(3)	0.28(9)	10.4(7)	2.299(1)	
	HFEPR	4.515(10)[e]	1.505(10)	0.333(3)	10.43(2)		2.384(2), 2.36(1), 2.47(5)
	INS				10.1(3)		
	AILFT-CASSCF	+6.97		0.055			2.437, 2.501, 2.509
	AILFT-NEVPT2	+4.42		0.107			2.316, 2.361, 2.373
	LFT				10.40,[b] 10.33[c]		
Co−I	DC susceptibility	+7.5(1)	0.11(10)	0.01(3)	15.0(1)	2.295(2)	
	HFEPR[f]	+6.1(5)	0.60(15)	0.10(3)	12.3(7)		2.55(10), 2.55(10), 2.35(10)
	INS				12.5(5)		
	AILFT-CASSCF	+9.70		0.197			2.482, 2.581, 2.627
	AILFT-NEVPT2	+7.24		0.193			2.335, 2.406, 2.437
	LFT				12.35,[b] 12.37[c]		

[a]The magnetic transition (at the $2D'$ value) for **Co−Cl** could not be confirmed in INS spectra, as it is at/below the detection limit (10 cm^{-1}) of the INS spectrometer VISION. [b]Calculated using e_σ and e_π parameters derived by comparison with experiments in ref 86. Complete parameters are provided in SI. [c]Calculated using e_σ and e_π parameters derived from AILFT calculations in ref 72, as discussed in the text. The result is provided in comparison with that in Footnote d. Complete parameters are provided in SI. [d]Crystal structure of $(NEt_4)_2[CoCl_4]$ (**Co−Cl**) is too disordered to be used for AILFT calculations. Thus, the calculations were only conducted on the $[CoCl_4]^{2-}$ anion in **Co−Cl**. [e]HFEPR results gave $|E/D| = 0.333$ for **Co−Br**. Thus, the simulated spectra for $D > 0$ and $D < 0$ are the same, as indicated in Figure 4 caption. No sign is given for D here. [f]The error values for spin-Hamiltonian parameters obtained by HFEPR are estimated from the line width for **Co−I**, unlike for **Co−Cl** and **Co−Br**.

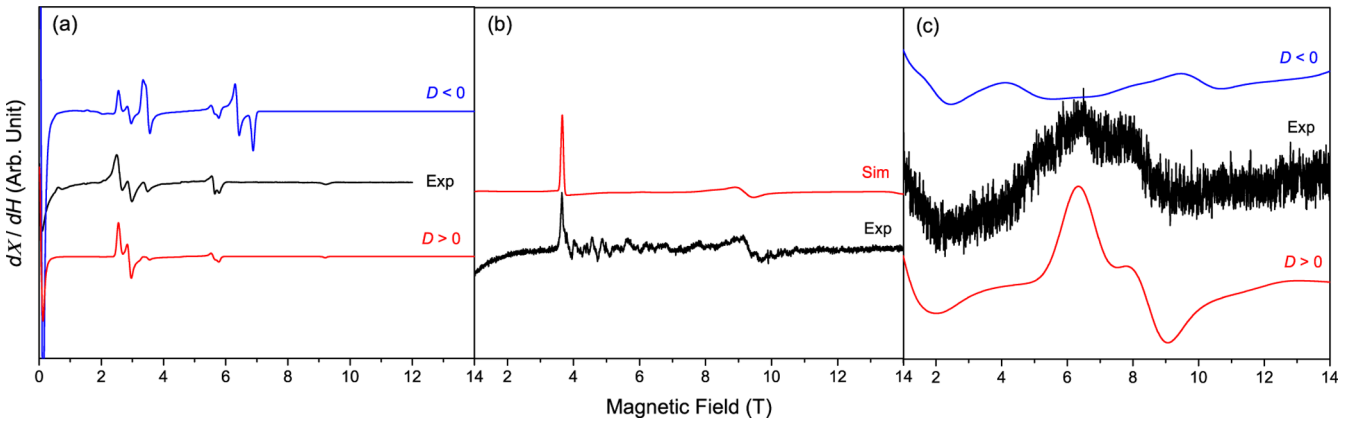

Figure 4. HFEPR spectra: (a) **Co−Cl** at 4.5 K and 148 GHz; (b) **Co−Br** at 4.5 K and 310 GHz; (c) **Co−I** at 4.5 K and 418 GHz. Since E/D = 0.333 for **Co−Br**, the simulated spectra for $D > 0$ and $D < 0$ are the same. dX/dH is the first derivative of the absorption X vs magnetic field H.

(intermolecular) and internal (intramolecular) vibrational modes in the solid states. Internal modes are molecular vibrations in which the molecules maintain almost no displacement of the mass center. External modes are lattice vibrations, when molecules vibrate primarily as a whole with little internal distortion and typically with much lower frequencies than internal modes. Internal and external modes are often coupled as they originate from the same governing equations. Thus, we do not distinguish external and internal modes in the current work and refer to all vibrations as phonons.

Variable-temperature (VT) INS spectra may distinguish magnetic from phonon transitions, as they have different temperature dependencies. Electrons (spin = 1/2) are fermions that follow the Boltzmann distribution (or Maxwell−Boltzmann statistics) at a given temperature. In contrast, phonons/vibrations (spin = 0) are bosons that follow Bose−Einstein statistics with temperature. In other words, magnetic and phonon peaks in VT INS spectra follow different temperature profiles. Bose correction of the INS spectra will bring phonon spectra at different temperatures to similar levels, thus helping reveal magnetic transitions.[94,106] Unlike IR and Raman spectroscopies, each with different selection rules to give IR-allowed and Raman-allowed transitions, respectively, INS has no symmetry-based selection rules for phonons. Hence, *all* phonon transitions are allowed in INS.[95,121]

INS experiments were conducted using Vibrational Spectrometer (VISION) at the Spallation Neutron Source (SNS), Oak Ridge National Laboratory (ORNL).[94,106] Variable-temperature INS can be used to distinguish between magnetic and phonon peaks due to their different temperature dependences. Bose correction of the VT INS spectra makes the intensities of phonon peaks relatively constant, helping to reveal magnetic peaks. Intensities of magnetic peaks decrease

https://doi.org/10.1021/acs.inorgchem.6c00405
Inorg. Chem. 2026, 65, 12818−12834

with increasing temperature, as the excited Kramers doublet in Figure 1 is increasingly thermally populated at the expense of the ground Kramers doublet.

VISION is an indirect-geometry INS spectrometer with its schematic shown in Figure 5. Such INS spectrometers have been reviewed.[94,106] An incident neutron beam (with energy E_i) with a broad range of energies (e.g., "white" beam) is used to irradiate the sample. The E_i is determined using the time the neutron reaches the detector through time-of-flight (TOF). Two banks of analyzers for forward- and backscattering of neutrons, respectively, are used to give spectra. Forward-scattering analyzers catch scattered neutrons with low Q (with respect to the incident neutron beam; Q = length of the vector of momentum transfer between the incident and outgoing neutrons).[94,106] Backscattering analyzers receive scattered neutrons with high Q. Magnetic transitions are more pronounced in forward-scattering with low Q, because their intensities decrease with increasing Q.[106] VT Bose-corrected forward scattering INS spectra of **Co−Br** (Figure 6a) show a prominent magnetic transition at 10.1(3) cm^{-1}, which is in good agreement with the HFEPR results. INS spectra of **Co−I** in (Figure 6c) reveal a broad magnetic transition at 12.5(5) cm^{-1} as opposed to a sharp transition in the INS spectra of **Co−Br**. The broadness of the peak in **Co−I** suggests the embedding of low-lying vibrations/phonons near the magnetic transition that could lead to spin-phonon couplings and fast relaxation as observed in the out-of-phase signal in AC susceptibility data for **Co−I** discussed below. The magnetic transition of **Co−Cl** at 4.5 cm^{-1} (from HFEPR) is below the lower detection limit of VISION (10 cm^{-1}).[94,106] INS also gives phonon (vibrational) spectra, which are presented for **Co−Cl**, **Co−Br**, and **Co−I** in Figures S8−S11 in SI over the range of 10−4000 cm^{-1}. These spectra show all phonon transitions, as INS has no symmetry-based selection rules.[95,121] As discussed below, DFT calculations give phonon energies in **Co−I** and their symmetries.

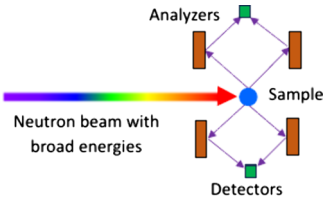

Figure 5. Schematic of VISION, an indirect-geometry INS spectrometer.

Ab Initio Ligand Field Theory (AILFT) Calculations

AILFT calculations have been performed using ORCA[122] to explore the electronic structures and magnetic anisotropies of the current compounds. Computational details are provided in SI. Due to the crystallographic disorders in the crystal structures of $(NEt_4)_2[CoX_4]$ (X = Br, **Co−Br**; I, **Co−I**), two calculations were conducted with and without the cation NEt_4^+, i.e., on $(NEt_4)_2[CoX_4]$ and $[CoX_4]^{2-}$, respectively. For $(NEt_4)_2[CoCl_4]$ (**Co−Cl**), its crystal structure is too disordered to be used for AILFT calculations. Thus, we only conducted AILFT calculations on the $[CoCl_4]^{2-}$ anion based on its structure in **Co−Cl**. Earlier, Vassilyeva and co-workers also conducted AILFT calculations on the $[CoCl_4]^{2-}$ fragment in the structure of $(C_{13}H_{12}N_3)_2[CoCl_4]$ ($C_{13}H_{12}N_3^+$ = 2-methyl-3-(pyridin-2-yl)imidazo[1,5-*a*]pyridinium).[123] Results of the current AILFT calculations are summarized in Table S3 in SI. Additional AILFT calculations have also been performed on $[CoBr_4]^{2-}$ and $[CoI_4]^{2-}$ anions, giving results summarized in SI (Table S6).

For **Co−Br** and **Co−I**, the calculated results are in good agreement with the experimental results. A pronounced effect of NEt_4^+ on anisotropy was observed in **Co−Br** and was minimal in the case of **Co−I**. The dominant contributions to the positive D values in $(NEt_4)_2[CoX_4]$ (**Co−Br** and **Co−I**) are from the first and second quartet states. In the case of **Co−Br**, the ground state consists 99.96% of $^4A_2$ in D_{2d} point group. In contrast, the ground and excited states of **Co−I** show several configurations, suggesting orbital contributions from the excited states. The relative energy orders of ligand field d-orbital splitting for **Co−Br** and **Co−I** were extracted according to ab initio ligand field theory (AILFT) analysis using NEVPT2 (Table S5).

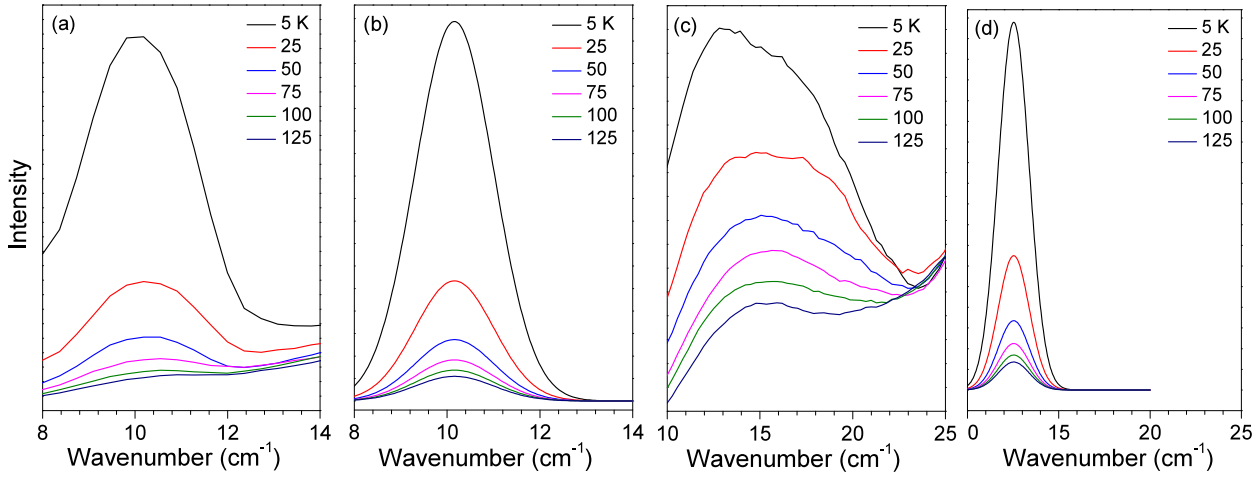

Figure 6. (a) VT forward-scattered, Bose-corrected INS spectra of **Co−Br** showing inter-Kramers (Ms = ±1/2 → ±3/2) magnetic transition at 10.1(3) cm^{-1}. (b) Calculated magnetic peaks in Bose-corrected INS spectra of **Co−Br** with $2D'$ = 10.1 cm^{-1} and the E/D ratio of 0.333 from HFEPR. (c) VT forward-scattered, Bose-corrected INS spectra of **Co−I** showing inter-Kramers (Ms = ±1/2 → ±3/2) magnetic transition at 12.5(5) cm^{-1}. (d) Calculated magnetic peaks in Bose-corrected INS spectra of **Co−I** with $2D'$ = 12.5 cm^{-1} and the E/D ratio of 0.1 from HFEPR.

https://doi.org/10.1021/acs.inorgchem.6c00405
Inorg. Chem. 2026, 65, 12818−12834

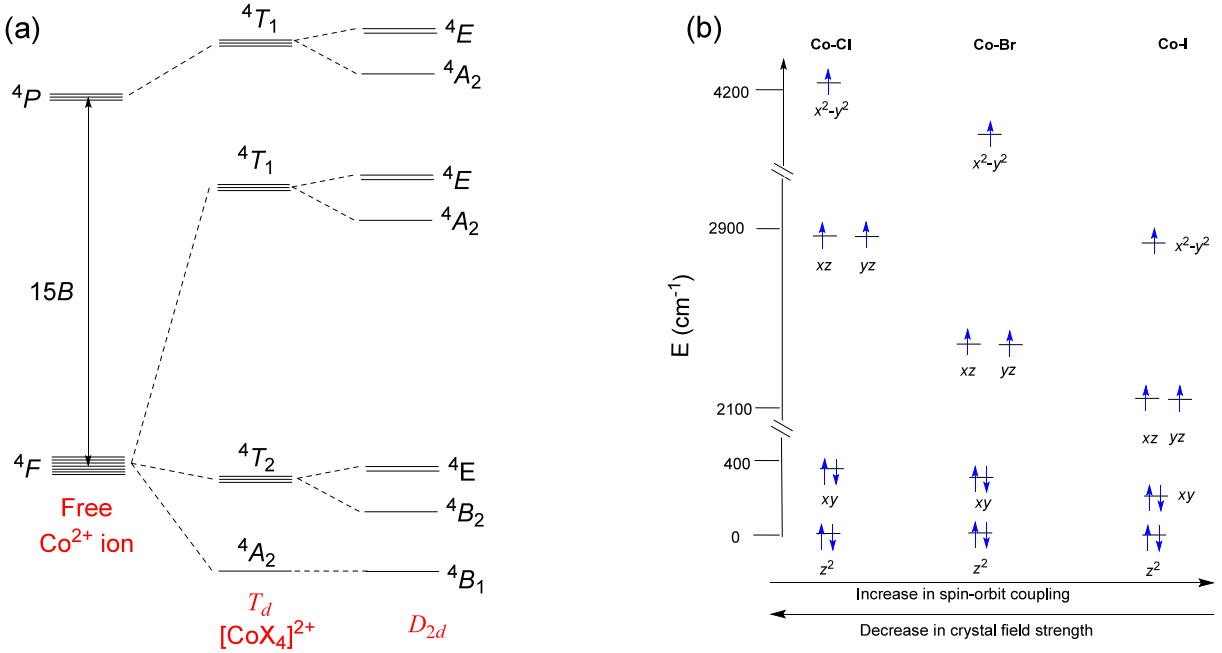

Figure 7. (a) Electronic states of free Co^{2+} ion, in a tetrahedral (T_d) and tetragonally compressed (D_{2d}) ligand field for **Co-X**. (b) d-orbital splitting from LFT calculation.

The AILFT calculations on the $[CoCl_4]^{2-}$ fragment in the structure of $(C_{13}H_{12}N_3)_2[CoCl_4]$ by Vassilyeva et al. gave a small and positive D value (3.96 cm^{-1}) with a moderate rhombic component (E/D = 0.12).[123] The ZFS obtained was small compared to that from experimental magnetometric determination, because it was based on a simple isolated ion model extracted from the ionic solid.[123] In current work, the overestimated D value of $[CoCl_4]^{2-}$ is likely associated with the high disorder in the crystal structure. However, E/D and g values show reasonable agreement with the experimental results. In an attempt to obtain a reasonable D value, the second d-shell (CAS 7,10) calculations were also conducted, in addition to using the Douglas−Kroll−Hess Hamiltonian (DKH) relativistic method. This still gave the same value as the one in Table 2. Thus, we think the overestimation of D is due to severe disorder in the crystal structure of **Co−Cl**.

Ligand Field Theory (LFT) Calculations of the Electronic Structures and ZFS Parameters

The origin of ZFS in these compounds was also probed with the semiempirical Angular Overlap Model (AOM) using the Ligfield program by J. Bendix,[124] and the locally written (J. Telser) program DDN.[125] Nover and Schmidtke reported the NIR (near IR) spectra of the three compounds from single crystals at 2 K and assigned Kramers components of the three quartet excited states, which in T_d are (in increasing energy): $^4T_2(F)$, $^4T_1(F)$, and $^4T_1(P)$. These states are split by spin-orbit coupling (SOC) and lower symmetry in the crystal. Assignment of electronic levels was by comparison with results from AOM calculations performed for various subgroup symmetries.[86] In the D_{2d} point group symmetry, the ground electronic state of **Co−X** is $^4B_1$, derived from the parent $^4A_2(F)$ term in T_d symmetry ($e^4t_2^3$ configuration). The quartet excited states are $^4T_2(F)$ ($e^3t_2^4$), $^4T_1(F)$ ($e^2t_2^5$), and $^4T_1(P)$ ($e^3t_2^4$) in T_d symmetry and each split into $^4B_2$ and ^4E for ($^4T_2$) or $^4A_2$ and ^4E (for $^4T_1$) states. Transitions to the states derived from $^4T_2$ and those derived from $^4T_1(F, P)$ are in the NIR and visible region, respectively, and have been reported from both experimental and theoretical perspectives.[86] These states are given in Figure 7a, showing the symmetry descent for the Co(II) ion from a free ion, first to a hypothetical tetrahedral $[CoX_4]^{2-}$ ion, and then to a hypothetical tetragonally compressed $[CoX_4]^{2-}$ ion in the present studies ($\theta_{1,2}$ > 54.5°) (Table S8a). The perturbation equation in eq 2, based on the second-order SOC and similar to the one given by Van Stapele et al., applies[126]

$$D = \left(\frac{4}{9}\right)\zeta^2\left[\frac{1}{E(^4E - {}^4B_1)} - \frac{1}{E(^4B_2 - {}^4B_1)}\right] \quad (2)$$

where ζ is the SOC constant for Co^{2+} ion, $E(^4B_2 - {}^4B_1)$ is the energy difference between the $^4B_2$ and $^4B_1$ states, and $E(^4E - {}^4B_1)$ is the energy difference between the ^4E and $^4B_1$ states.

Angular overlap model (AOM) parameters e_σ and e_π for the **Co−Cl** and **Co−Br** complexes were taken directly from Benelli and Gatteschi.[85] For **Co−I**, e_σ and e_π were not reported and were therefore determined in two ways: (a) e_σ = 2800, e_π = 820 cm^{-1} were treated as adjustable parameters and optimized jointly with the SOC constant ζ to reproduce the experimental ZFS, while preserving the expected spectrochemical trend of a weaker ligand field for iodide; (b) e_σ and e_π were extrapolated by scaling with the halide ionic radii (1.96 Å for Br^- and 2.20 Å for I^-; scaling factor = 1.122), which yields e_σ^I = 3478 cm^{-1}, e_π^I = 870 cm^{-1}, using e_σ^{Br} = 3100 and e_π^{Br} = 775 cm^{-1}. The Racah parameter B for **Co−Br** (695 cm^{-1}) was adopted from Schmidtke,[86] whereas B for **Co−Cl** (700 cm^{-1}) and **Co−I** (690 cm^{-1}) was adjusted to reflect the expected nephelauxetic trend of decreasing interelectronic repulsion along Cl < Br < I; the corresponding C = ~4.3B values were then scaled, together with B, to approximately 70% of the Co^{2+} free-ion value (B = 988.6 cm^{-1})[127] to account for overall metal−ligand covalency. Spin-orbit coupling was included via effective one-electron SOC constants ζ, which were adjusted for each **Co−X** complex to reproduce the experimental ZFS

https://doi.org/10.1021/acs.inorgchem.6c00405
Inorg. Chem. 2026, 65, 12818−12834

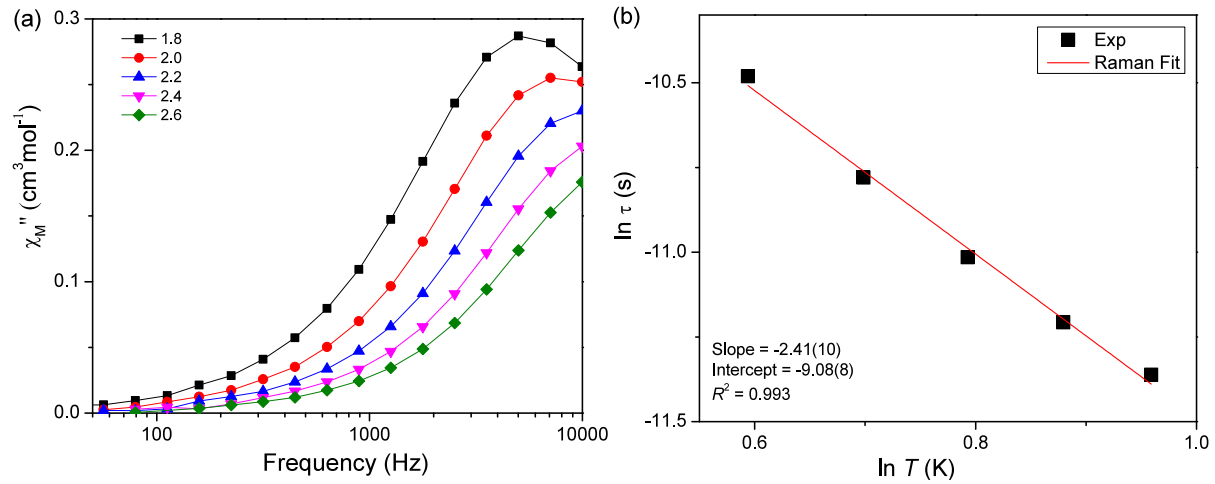

Figure 8. (a) Frequency-dependent out-of-phase AC susceptibility at 1.8−2.6 K under 0.1 T static DC field for **Co−Cl**. (b) ln τ vs ln T plot for **Co−Cl**. The red solid line represents the fit by the Raman relaxation process.

parameters (Table 2); relative to the Co^{2+} free-ion value (ζ_{free} = 533 cm^{-1}),[128] the fitted ζ values are 243 cm^{-1} (**Co−Cl**, 46%), 300 cm^{-1} (**Co−Br**, 56%), and 385 cm^{-1} (**Co−I**, 72%). These calculated ZFS values with a positive sign corroborate the HFEPR results for the compounds (Table 2). The ZFS values increase with an increase in the (second-order) SOC, a decrease in the crystal field parameters (Figure 7b), and the σ bond strength (e_σ) Cl > Br > I, which are in agreement with the spectrochemical series.[129] In addition to the sign and magnitude of ZFS, the calculations also gave the single d-orbital energy splitting in Figure 7b. AOM parameters e_σ and e_π obtained from AILFT by Buchhorn, Deeth, and Krewald were also employed as an independent theoretical reference set.[72] Using these AILFT-derived AOM parameters, together with the Racah parameters and ζ values defined above and the experimental geometries, leads to an overestimation of the axial ZFS parameter $2D'$. However, a good agreement with the experimental $2D'$ was achieved by reducing ζ, such that the required ζ values amount to 38, 47, and 63% of the free-ion value (533 cm^{-1}) for **Co−Cl**, **Co−Br**, and **Co−I**, respectively (Tables S8−S10). The systematic increase in the fitted SOC ζ from Cl to Br to I reflects the larger atomic spin-orbit coupling of the heavier halides and is consistent with their higher covalency, as expected from the nephelauxetic effect. The calculations using the AILFT-based parameters show the plausible B, C, and ζ ranges to give $2D'$ values comparable with those from HFEPR experiments.

Dynamic Magnetic Properties

Spin-lattice relaxation refers to the process by which the spin system of magnetic ions or complexes equilibrates with the lattice vibrations (phonons) at thermal equilibrium, which may be influenced by the crystallographic symmetry of the material. A long relaxation time to spin reversal is desired for SMMs in data storage applications. The spin and lattice systems are the components of SMMs, and interactions between them are often termed spin-phonon couplings, leading to relaxations.[10] Equation 3 shows the three types of spin-lattice relaxation mechanisms:

$$\tau^{-1} = AH^{n_1}T + CT^{n_2} + \tau_0^{-1}\exp^{(-U_{eff}/k_BT)} \quad (3)$$

where the first term represents the direct process, the second term is Raman process, and the third term describes the thermally activated Orbach process. τ^{-1} = rate of spin reversal; A = direct process constant; H = magnetic field; T = temperature; C = Raman constant; τ_0 = relaxation time; U_{eff} = energy to spin reversal; k_B = Boltzmann constant.

The dynamic magnetic properties of the compounds were probed by AC susceptibility studies at 10 kHz frequency under an applied 0.1 T DC field. The applied DC field is required to quench quantum tunneling and to give an observable out-of-phase signal, which is often used for Co(II) complexes.[130] The results showed that both **Co−Cl** and **Co−Br** exhibit SMM properties. Due to the 10 kHz frequency limit for the current state-of-the-art SQUID instrument, **Co−Cl** shows three maxima points below 10 kHz (Figure 8a). Maxima points at two additional temperatures (2.4, 2.6 K) were also obtained based on the data <10 kHz using the *CCFit2* program.[131,132] Since these two maxima points were essentially obtained through extrapolation, their use in Figure 8b should be viewed with caution. In addition, the temperature range of 1.8−2.6 K is small, potentially leading to large errors. The ln τ vs ln T plot in Figure 8b gives a linear fit (R^2 = 0.997) with C = 8.8(9) × 10^3 s^{-1} and n_2 = 2.41(10). The relaxation dynamics is interpreted using the Raman mechanism, since the data points were obtained at lower temperatures. n_2 is lower than 9 expected for the Raman pathway, but it is consistent with the presence of the phonon-bottleneck effect. Cole−Cole plots for **Co−Cl** are given in Figure S5a in the SI. However, **Co−Br** shows only one data point below 10 kHz (Figure S3), which is not sufficient to fit the Debye equation.

Co−I (with the largest D value) does not show an out-of-phase signal in the AC measurements. **Co−I** crystallizes in the orthorhombic $P2_12_12$ (No. 18) space group with the D_2 point group symmetry ($x \neq y \neq z$),[133] while **Co−Cl** and **Co−Br** crystals are in the tetragonal space group $P4_2/nmc$ (No. 137) and $P\text{-}42_1c$ (No. 114) with the D_{4h} and D_{2d} point group symmetries ($x = y \neq z$), respectively.[134] Thus, phonons have the degenerate E_g and E_u modes for **Co−Cl** or the E mode for **Co−Br**, while those in **Co−I** have no degenerate modes (only A or B_1, B_2, B_3, Table S13 in SI). In other words, there are fewer phonon modes in **Co−Cl** and **Co−Br** due to their degeneracy than in **Co−I**. We speculate that, as a result, spin-phonon couplings are more likely in **Co−I**, leading to its magnetic relaxation.

https://doi.org/10.1021/acs.inorgchem.6c00405
Inorg. Chem. 2026, 65, 12818−12834

Spin-Phonon Couplings in FIRMS and Selected Phonons in Co−I by VASP Calculations

FIRMS is far-IR spectroscopy inside magnetic fields, a crucial technique for investigating magnetic properties and spin-phonon interactions. In the experiments, far-IR spectra at different magnetic fields are collected, revealing how Zeeman splitting shifts magnetic transitions.[17,23,28,31,34,135−148] In the present case, it provides direct measurements of $2D'$ values for $S = 3/2$ spin state, and may reveal spin-phonon couplings typically as avoided crossings, offering insight into the spin relaxation process.[94,86] Earlier research by Brackett, Richards, and co-workers demonstrated that transitions between ZFS states are magnetic dipole-allowed, with the transition moment operator (R_x, R_y, R_z).[149]

Magnetic transitions of the three **Co−X** compounds (at $2D'$ in Table 2) are either outside or at the low detection limit (typically 12 cm^{-1}) of the FIRMS instrument at NHMFL.[34,94] Thus, FIRMS did not directly show the magnetic transitions in **Co−X** at 0 T. However, in the FIRMS of **Co−I** (Figure 9),

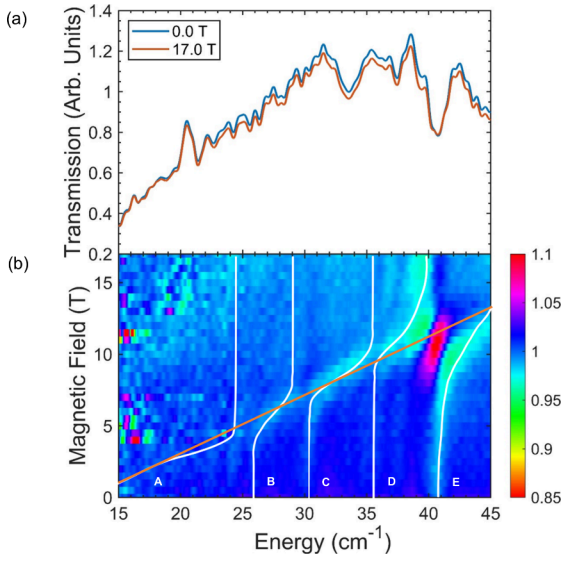

Figure 9. (a) Far-IR spectra of **Co−I** at 0 and 17 T, the lowest and highest magnetic field, respectively, revealing changes in the spectrum by the fields. (b) Contour plot of the normalized far-IR spectra at 0−17 T (step: 1 T; normalization by the average of all spectra), showing spin-phonon couplings with the Maple software. White lines indicate fittings from eq 4 corresponding to coupling of the magnetic transition **A** to phonons **B**, **C**, **D**, and **E**. Fitting parameters are shown in Table 3. The brown line shows the blue-shift of the magnetic transition.

several spin-phonon couplings were observed involving low-energy phonons. Observation of these couplings, demonstrated as avoided crossings, is consistent with the faster spin-relaxation observed in **Co−I** than in **Co−Cl** and **Co−Br** by dynamic (AC) susceptibility. The $M_S = -1/2$ to $M_S = +3/2$ magnetic transition, which is extrapolated to 12.5 cm^{-1} at 0 T and labeled **A** in Figure 9, undergoes a blue-shift (i.e., shift to higher energies) with magnetic field increase. Due to the presence of transverse or rhombic anisotropy E leading to admixture of states shown in Figure 1, this transition has the $M_S = -1/2 \rightarrow M_S = -1/2$ ($\Delta M_S = 0$) component and is spin-allowed. In FIRMS of **Co−Br** (Figure S12 in SI), a similar $M_S = -1/2$ to $M_S = +3/2$ magnetic transition, extrapolated to 10.4 cm^{-1} at 0 T ($2D'$), is also observed. This transition undergoes a blue shift with magnetic field increase, although no spin-phonon coupling is obvious in the plots (Figure S12).

In FIRMS of **Co−I** (Figure 9), the interaction of magnetic transitions (spin) with a phonon is observed as an avoided interaction with the magnetic transition taking up phonon character and the phonon becoming magnetic with an increase in field. When the energy of a phonon is close to the magnetic excitation, spin-phonon coupling occurs, in which the phonon peak appears to be "pushed" away from the magnetic peak. Such coupling is often expressed with a simple Hamiltonian in eq 4:

$$H = \begin{pmatrix} E_{sp} & \Lambda \\ \Lambda & E_{ph} \end{pmatrix} \tag{4}$$

Understanding spin-phonon interaction is a crucial aspect of developing better SMMs. This requires simulation of the interaction between magnetic transition and possible phonons which can be performed using the given Hamiltonian in Maple software. This method yields the diagonal matrix element corresponding to the expected shift in magnetic and phonon transitions with the field, and the off-diagonal element, Λ, corresponding to the spin-phonon coupling constant.

In **Co−I**, four phonons, labeled **B**, **C**, **D**, and **E** in Figure 9, were found to interact with the magnetic transition, resulting in a Hamiltonian as a 5 × 5 matrix representation in eq 5 under the assumption that there is no phonon−phonon interaction. Fitting eq 5 gives the simulated spin-phonon lines in Figure 9 and the four spin-phonon coupling constants Λ_B−Λ_E in Table 3. Phonon **B** at 25 cm^{-1} initially shows magnetic field dependence until ∼4 T, when it begins to exhibit avoided crossing behavior, acquiring magnetic character, while the magnetic transition correspondingly becomes phonon-like. This coupled state then continues as a magnetic excitation until it interacts with Phonon **C** at 30 cm^{-1} at ∼8 T, leading to another avoided crossing. **C** gradually becomes a phonon, while Phonon **D** takes more magnetic character, blue-shifting to the right. The process repeats at about 10 T, when **D** undergoes a third avoided crossing with Phonon **E** at 42 cm^{-1}.

Table 3. Energies of Phonons B, C, D, and E in Co−I, Their Symmetries, and Spin-Phonon Coupling Constants Λ_B−Λ_E

	A (spin)	B	C	D	E
energy (cm^{-1})	12.3	25.9	30.2	35.6	40.8
VASP-calculated phonons (cm^{-1})[a]		25.99	30.76	35.85	40.34
symmetry of the calculated phonons		B_1	B_2	B_3	B_2
coupling constants Λ_B, Λ_C, Λ_D, Λ_E (cm^{-1})		0.5	0.5	0.5	0.5

[a]These VASP-calculated, IR-active phonons are the closest in energy to Phones **B**−**E**. However, they are not necessarily Phones **B**−**E**.

$$H = \begin{pmatrix} E_{sp} & \Lambda_B & \Lambda_C & \Lambda_D & \Lambda_E \\ \Lambda_B & E_{phB} & 0 & 0 & 0 \\ \Lambda_C & 0 & E_{phC} & 0 & 0 \\ \Lambda_D & 0 & 0 & E_{phD} & 0 \\ \Lambda_E & 0 & 0 & 0 & E_{phE} \end{pmatrix} \tag{5}$$

https://doi.org/10.1021/acs.inorgchem.6c00405
Inorg. Chem. 2026, 65, 12818−12834

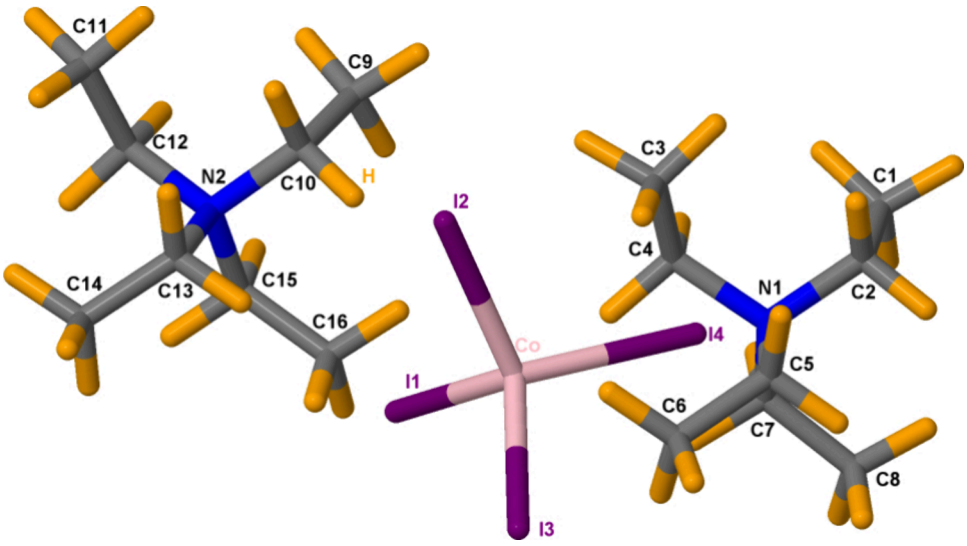

Figure 10. Molecular structure of **Co−I** with labels of C (gray color), N (blue), H (orange), Co (pink), and I (purple) atoms for the discussion of phonons, including the movies given in SI.

VASP (Vienna Ab initio Simulation Package) calculations using density functional theory (DFT)[150] can provide the phonon symmetries and energies for a given compound as well as phonon movies.[26,27,30,33,150] The VASP calculations were only conducted on **Co−I**, as the NEt_4^+ cations in the crystal structures of both **Co−Cl** and **Co−Br** are too disordered to be used in the calculations. Calculated phonon symmetries and energies are listed in Table S14 in SI. Since B_1, B_2, and B_3 modes are IR-active in D_2 point group (Table S13), and Phonons **B**, **C**, **D**, and **E** in FIRMS are in the energy range of 25−42 cm^{-1}, 21 VASP-calculated movies of B_1, B_2, and B_3 modes in 20−45 cm^{-1} are presented in SI. These movies show the IR-active phonons within the crystallographic unit cell, including both intra- and intermolecular vibrations. In addition, four of the 21 calculated IR-active phonons, whose energies (at 25.99, 30.76, 35.85, and 40.34 cm^{-1}) are the closest to Phonons **B**, **C**, **D**, and **E**, respectively, are selected for discussion below. Their movies of intramolecular vibrations (with just one molecule in the cell similar to that in Figure 10) are also given in SI for the discussion of phonon features.

The calculated phonon at 25.99 cm^{-1} with B_1 symmetry is close in energy to Phonon **B**. This vibrational mode is primarily localized on the NEt_4^+ cations, particularly in the terminal CH_3 groups. Asymmetric C−H stretching and torsional motions are observed in CH_3 groups attached to C1 and C3 atoms, which twist in the same direction but with different magnitudes. This contrasts with the CH_3 stretching of C7 and C11 atoms, which move in the opposite directions. The N−C framework exhibits slight bending toward the metal center. A wagging motion of the Co−I bonds is also evident, confirming that this mode involves distortion of the first coordination sphere around the Co center.

The calculated phonon at 30.76 cm^{-1} with B_2 symmetry is close in energy to Phonon **C**. In this vibration, the torsional and wagging of the CH_3 groups attached to C1 and C3 atoms are still the same as the phonon at 25.99 cm^{-1}, except that the CH_3 groups of C9, C11, and C16 atoms are in the opposite directions with a larger amplitude. The wagging of the **Co−I** core is observable.

The calculated phonon at 35.85 cm^{-1} with B_3 symmetry is close in energy to Phonon **D**. This vibration represents a symmetric wagging of the ethyl groups on each of the NEt_4^+ cations, with opposing displacements at the two N centers. The Co−I stretching is weaker than that of phonon at 30.76 cm^{-1}.

The calculated phonon at 40.34 cm^{-1} with B_2 symmetry is close in energy to Phonon **E**. This molecular vibration involves the bending (scissor-like) motion of the alkyl substituents. The deformation propagates through the C−C and C−N framework, which acts as a hinge, resulting in collective NEt_4^+ distortion. The **Co−I** core has a minimal wagging motion.

CONCLUSIONS

The current work provides detailed studies of magnetism in the $(NEt_4)_2[CoX_4]$ series (X = Cl, **Co−Cl**; X = Br, **Co−Br**; X = I, **Co−I**). These compounds with near T_d geometry about the Co(II) ions provide an insight into how the crystal field and crystallographic point groups impact their ZFS values and spin relaxation. An increase in D values was observed from **Co−Cl** to **Co−I** due to a rise in spin-orbit coupling (SOC) and a decrease in crystal field splitting in the complexes, allowing for more mixing of d-orbitals and increased ZFS. The crystallographic point groups and molecular structures in the crystals appear to be prominent factors in spin relaxation. **Co−Cl** and **Co−Br** are in more symmetric tetragonal space groups, while **Co−I** is in a less symmetric orthorhombic group, leading to more complicated splitting, the largest ZFS, and the fastest spin relaxation. This observed trend was also validated from INS and FIRMS data, with INS data showing a broad peak and FIRMS showing several avoided spin-phonon couplings in **Co−I**. Additionally, the primary mass effect, **Co−Cl** < **Co−Br** < **Co−I,** becomes appreciable, leading to potentially more low-lying phonons that could interact with the spins, leading in turn to an increase in relaxation in the series. Data from HFEPR, DC magnetic susceptibility fitting, and AILFT and LFT calculation gave a reasonable agreement. The results from this work on a simple series of homoleptic complexes can give an insight into the factors to manipulate toward making a good candidate for SMM applications.

https://doi.org/10.1021/acs.inorgchem.6c00405
Inorg. Chem. 2026, 65, 12818−12834

EXPERIMENTAL SECTION

Synthesis of Co-X Complexes

The complexes $(NEt_4)_2[CoX_4]$ (**Co-X**; X = Cl, Br, I) were prepared by the literature methods.[151] The UV−vis spectra were recorded at room temperature in acetonitrile using an Agilent UV−visible spectrometer.

Single-Crystal X-ray Diffraction

Single-crystal X-ray diffraction data were collected using a Bruker D8 Venture at 100 K with Mo K_α radiation using φ and ω scans. Data collection and integration were completed using APEX 4 programs, reduced using Bruker SAINT, and corrected for absorption using the SADABS multiscan program.[152,153] Molecular structure models were solved using SHELXT and refined with SHELXL, using the OLEX2−1.5 interface.[154−156]

DC/AC Magnetic Susceptibility Measurements

Magnetic measurements were performed using a vibrating sample magnetometer (VSM) of the Quantum Design MPMS SQUID-VSM system. Variable-temperature DC susceptibility data of these compounds were collected under a field of 0.10 T in the range of 1.8−300 K. Alternating-current (AC) susceptibility measurements were carried out on a vibrating sample magnetometer (VSM) of Quantum Design PPMS system with an oscillating AC field of 1000 Oe for **Co−Cl** and **Co−Br** and 3000 Oe for **Co−I**, respectively, at frequencies ranging from 10 to 10,000 Hz. All magnetic susceptibility data were corrected for the diamagnetic contributions of the sample holder as well as for the diamagnetism of the sample using Pascal's constants.[157]

The DC and AC data were processed using the *PHI* program[91] and the *CCFit2* program,[131,132] respectively.

HFEPR and FIRMS Measurement

HFEPR was performed at the EMR facility at NHMFL. The facility operates a transmission spectrometer described elsewhere,[158] which was modified by the use of Virginia Diodes Inc. (VDI, Charlottesville, VA, USA) sources, generating sub-THz radiation in the 50−640 GHz frequency range. The spectrometer is associated with a 15/17 T warm-bore superconducting magnet. The samples were measured both "as is" which allowed them to orient (torque) in the magnetic field, or as pellets mixed with *n*-eicosane. About 30−60 mg of the powder samples were used in each measurement.

FIRMS spectra were recorded at the National High Magnetic Field Laboratory (NHMFL) using a Bruker Vertex 80v FT-IR spectrometer with a 17.5 T superconducting magnet. A mercury lamp and a composite silicon bolometer served as the THz radiation source and detector. The radiation traveled through an evacuated optical beamline and a brass light pipe to minimize air absorption, reaching the sample at the field center. Samples, prepared as *n*-eicosane mulls with ∼2 mg of powder, were cooled to ∼5 K alongside the bolometer using helium gas. Spectra were measured from 10 to 720 cm^{-1} (0.3−21.6 THz) with 0.3 cm^{-1} resolution, a 4 min acquisition time, and a scanner speed of 20 kHz.

Inelastic Neutron Scattering (INS)

Variable-temperature inelastic neutron scattering (INS) spectra were recorded using the Vibrational Spectrometer (VISION) at the Spallation Neutron Source (SNS), ORNL. Approximately 0.5 g of powdered sample was sealed in an aluminum can, mounted on a sample holder, and positioned within the neutron beam. INS spectra at 5, 25, 50, 75, 100, and 125 K were collected and analyzed. INS spectra of **Co−X** in the 10−4000 cm^{-1} range at 5 K is shown in Figures S8−S11. The magnetic regions of the variable-temperature (VT) INS spectra of **Co−Br** and **Co−I** are given in Figure 6.

Ab Initio Ligand Field Theory (AILFT) Calculations

AILFT calculations were carried out using the ORCA software package (version 5.0.4).[159] Computational models were based on crystallographic structures of **Co−Cl**, **Co−Br**, and **Co−I** obtained in the current work. Zora-def2-TZVP was used for Co and X = Cl, Br, while sarc-zora-def2 was used for I. The resolution of identity and chain of sphere (RIJCOSX) approximations[160] were applied in conjunction with the appropriate auxiliary basis sets.[161] The core orbitals were not frozen. For the three complexes, the CAS(7,5) active space and 10 quartets and 40 doublets were calculated. Dynamic electron correction was incorporated using N-electron valence state second-order perturbation theory (NEVPT2).[162] Parameters related to spin-orbit coupling (*g*-values and ZFS) were calculated by calling the SINGLE ANISO program.

Ligand Field Theory (LFT) Calculations

LFT calculations were obtained using Ligfield software by Bendix[124] and the locally written DDN software by Telser.[125] The experimental data were satisfactorily fitted using the AOM parameters in SI. For simplification, halide ligands were considered equivalent across all compounds and were assumed to exhibit cylindrical π-donating interactions. The DDN software can incorporate the effects of an external magnetic field. Applying a magnetic field of 300 mT, like that used in conventional X-band EPR, helps reveal the spin states of the compounds and provides information about the sign of *D*, and can also get the *g* values from the slope of the lines with multiple fields.

The DDN software can also take as input the single electron d orbital energies (either as the five pure d orbitals or the 5 × 5 d orbital matrix) and these values were taken from the AILFT calculations to calculate ZFS in the **Co−X** series (Table S12).

DFT Phonon Calculations

Modeling by spin-polarized Density Functional Theory (DFT) was performed using the Vienna Ab initio Simulation Package (VASP).[163] The calculation used Projector Augmented Wave (PAW) method[164,165] to describe the effects of core electrons, with an energy cutoff of 800 eV for the plane-wave basis of the valence electrons. The lattice parameters and atomic coordinates from the CIF file, generated by the single-crystal X-ray diffraction measurement of **Co−I** at 100 K, were used as the initial structure. Given the relatively large unit cell (252 atoms), the electronic structure was calculated on the Γ-point only. The total energy tolerance for electronic energy minimization was 10^{-8} eV, and 10^{-7} eV for structure optimization. The maximum interatomic force after relaxation was below 0.001 eV/Å. The optB86b-vdW functional[166,167] for dispersion corrections was applied, and a Hubbard U term of 3.32 eV[168] was applied to account for the localized Co 3*d* orbitals. The vibrational eigenfrequencies and modes were then calculated using VASP and Phonopy.[169] The OClimax software[170] was used to convert the DFT-calculated phonon results to the simulated INS spectra.

ASSOCIATED CONTENT

Supporting Information

The Supporting Information is available free of charge at https://pubs.acs.org/doi/10.1021/acs.inorgchem.6c00405.

Additional movies of four IR-active phonons at 25.99, 30.76, 35.85, and 40.34 cm^{-1} showing one molecule in the crystal unit cell (ZIP)

Movies of VASP-calculated, IR-active phonons of **Co−I** in the 20−45 cm^{-1} range (ZIP)

Author contributions, table of single-crystal X-ray diffraction, IR spectra of **Co−X**, electronic spectra of **Co−X**, additional DC and AC results, additional HFEPR results, INS spectra in the 10−4000 cm^{-1} range, additional FIRMS and far-IR results, additional results from the AILFT and LFT calculations, and calculated phonon modes in **Co−I** and their symmetries (PDF)

Accession Codes

Deposition Numbers 2525231−2525233 contain the supplementary crystallographic data for this paper. These data can be obtained free of charge via the joint Cambridge Crystallo-

https://doi.org/10.1021/acs.inorgchem.6c00405
Inorg. Chem. 2026, 65, 12818−12834

graphic Data Centre (CCDC) and Fachinformationszentrum Karlsruhe Access Structures service.

AUTHOR INFORMATION

Corresponding Author

Zi-Ling Xue − *Department of Chemistry, University of Tennessee, Knoxville, Tennessee 37996, United States;* orcid.org/0000-0001-7401-9933; Email: xue@utk.edu

Authors

Adiat A. Fakolujo − *Department of Chemistry, University of Tennessee, Knoxville, Tennessee 37996, United States;* orcid.org/0009-0007-1742-5426

Michael J. Jenkins − *Department of Chemistry, University of Tennessee, Knoxville, Tennessee 37996, United States*

J. Krzystek − *National High Magnetic Field Laboratory, Florida State University, Tallahassee, Florida 32310, United States;* orcid.org/0000-0001-6088-1936

You Song − *State Key Laboratory of Coordination Chemistry, School of Chemistry and Chemical Engineering, Nanjing University, Nanjing 210023, China;* orcid.org/0000-0002-0289-7830

Xiaoping Wang − *Neutron Scattering Division, Oak Ridge National Laboratory, Oak Ridge, Tennessee 37831, United States;* orcid.org/0000-0001-7143-8112

Yongqiang Cheng − *Neutron Scattering Division, Oak Ridge National Laboratory, Oak Ridge, Tennessee 37831, United States;* orcid.org/0000-0002-3263-4812

Luke L. Daemen − *Neutron Scattering Division, Oak Ridge National Laboratory, Oak Ridge, Tennessee 37831, United States*

Mykhaylo Ozerov − *National High Magnetic Field Laboratory, Florida State University, Tallahassee, Florida 32310, United States;* orcid.org/0000-0002-5470-1158

Joshua Telser − *Department of Biological, Physical, and Health Sciences, Roosevelt University, Chicago, Illinois 60605, United States;* orcid.org/0000-0003-3307-2556

Zhao-Bo Hu − *Jiangxi Provincial Key Laboratory of Functional Crystalline Materials Chemistry, School of Chemistry and Chemical Engineering, Jiangxi University of Science and Technology, Ganzhou 34100, China;* orcid.org/0000-0001-9266-6624

Complete contact information is available at: https://pubs.acs.org/10.1021/acs.inorgchem.6c00405

Notes

The authors declare no competing financial interest.

ACKNOWLEDGMENTS

A.A.F. and Z.L.X. thank the US National Science Foundation (CHE-2055499 and CHE-2349345) for support of the research. Any opinions, findings, and conclusions expressed in this material are those of the authors and do not necessarily reflect the views of the US National Science Foundation. The National Natural Science Foundation of China (22373048) is acknowledged for the measurement of both DC and AC (10,000 Hz) magnetic susceptibility data. Part of this work was performed at the National High Magnetic Field Laboratory (NHMFL), which is supported by NSF Cooperative Agreement No. DMR-2128556 and the State of Florida. Neutron scattering experiments were conducted at the Spallation Neutron Source, which is supported by the Scientific Users Facilities Division, Office of Basic Energy Sciences, U.S. Department of Energy under Contract DE-AC0500OR22725 with UT Battelle, LLC. This research used computing resources made available through the VirtuES project, funded by the Laboratory Directed Research and Development program and Compute and Data Environment for Science (CADES) at ORNL, as well as resources of the National Energy Research Scientific Computing Center (NERSC), a U.S. Department of Energy Office of Science User Facility located at Lawrence Berkeley National Laboratory, operated under Contract No. DE-AC02-05CH11231 using NERSC award ERCAP0024340. AAF and ZLX acknowledge the Infrastructure for Scientific Applications and Advanced Computing (ISAAC) at the University of Tennessee for computational resources. We thank Dr. Tianwei Wang, Nanjing University, China, for help with the collection of the DC and AC magnetic susceptibility data, Prof. Jesper Bendix, University of Copenhagen, Denmark, for the Ligfield software, Prof. Daniel Aravena, University of Santiago, Chile, for help with the ORCA software, Dr. Andrew Ozarowski, NHMFL, for the SPIN software, and Dr. Adam T. Hand for the MATLAB script for processing the FIRMS data.

REFERENCES

(1) Hill, S. Magnetization tunneling in high-symmetry Mn_{12} single-molecule magnets. *Polyhedron* **2013**, *64*, 128−135.

(2) Aravena, D.; Ruiz, E. Spin dynamics in single-molecule magnets and molecular qubits. *Dalton Trans.* **2020**, *49*, 9916−9928.

(3) Zabala-Lekuona, A.; Seco, J. M.; Colacio, E. Single-Molecule Magnets: From Mn_{12}-ac to dysprosium metallocenes, a travel in time. *Coord. Chem. Rev.* **2021**, *441*, No. 213984.

(4) Bar, A. K.; Pichon, C.; Sutter, J.-P. Magnetic Anisotropy in Two- to Eight-Coordinated Transition-Metal Complexes: Recent Developments in Molecular Magnetism. *Coord. Chem. Rev.* **2016**, *308*, 346−380.

(5) Benelli, C.; Gatteschi, D. *Introduction to Molecular Magnetism: From Transition Metals to Lanthanides*; John Wiley & Sons, 2015.

(6) Perlepe, P. S.; Maniaki, D.; Pilichos, E.; Katsoulakou, E.; Perlepes, S. P. Smart Ligands for Efficient 3d-, 4d- and 5d-Metal Single-Molecule Magnets and Single-Ion Magnets. *Inorganics* **2020**, *8*, 39.

(7) Shao, D.; Wang, X.-Y. Development of Single-Molecule Magnets. *Chin. J. Chem.* **2020**, *38*, 1005−1018.

(8) Feng, M.; Tong, M.-L. Single Ion Magnets from 3d to 5f: Developments and Strategies. *Chem.—Eur. J.* **2018**, *24*, 7574−7594.

(9) Ruamps, R.; Maurice, R.; Batchelor, L.; Boggio-Pasqua, M.; Guillot, R.; Barra, A. L.; Liu, J.; Bendeif, E.-E.; Pillet, S.; Hill, S.; Mallah, T.; Guihéry, N. Giant Ising-Type Magnetic Anisotropy in Trigonal Bipyramidal Ni(II) Complexes: Experiment and Theory. *J. Am. Chem. Soc.* **2013**, *135*, 3017−3026.

(10) Frost, J. M.; Harriman, K. L. M.; Murugesu, M. The rise of 3-d single-ion magnets in molecular magnetism: towards materials from molecules? *Chem. Sci.* **2016**, *7*, 2470−2491.

(11) Sarkar, A.; Dey, S.; Rajaraman, G. Role of Coordination Number and Geometry in Controlling the Magnetic Anisotropy in Fe^{II}, Co^{II}, and Ni^{II} Single-Ion Magnets. *Eur. J. Chem.* **2020**, *26*, 14036−14058.

(12) Tupolova, Y. P.; Shcherbakov, I. N.; Korchagin, D. V.; Tkachev, V. V.; Lebedev, V. E.; Popov, L. D.; Zakharov, K. V.; Vasiliev, A. N.; Palii, A. V.; Aldoshin, S. M. Fine-Tuning of Uniaxial Anisotropy and Slow Relaxation of Magnetization in the Hexacoordinate Co(II) Complexes with Acidoligands. *J. Phys. Chem. C* **2020**, *124*, 25957−25966.

(13) Wang, X.-Y.; Avendaño, C.; Dunbar, K. R. Molecular Magnetic Materials Based on 4d and 5d Transition Metals. *Chem. Soc. Rev.* **2011**, *40*, 3213−3238.

(14) Zhuo, Z.; Li, G.-L.; Huang, Y.-G. In: *Advanced Strucutral Chemistry*, ed. Cao, R., 2021, vol. 2, ch. 13, pp 777−832.
(15) Tin, P.; Bone, A. N.; Bui, N. N.; Zhang, Y.-Q.; Chang, T.; Moseley, D. H.; Ozerov, M.; Krzystek, J.; Cheng, Y.; Daemen, L. L.; Wang, X.; Song, L.; Chen, Y.-S.; Shao, D.; Wang, X.-Y.; Chen, X.-T.; Xue, Z.-L. Advanced Spectroscopic and Computational Studies of a Cobalt(II) Coordination Polymer with Single-Ion-Magnet Properties. *J. Phys. Chem. C* **2022**, *126*, 13268−13283.
(16) Ferrando-Soria, J.; Vallejo, J.; Castellano, M.; Martínez-Lillo, J.; Pardo, E.; Cano, J.; Castro, I.; Lloret, F.; Ruiz-García, R.; Julve, M. Molecular magnetism, quo vadis? A historical perspective from a coordination chemist viewpoint. *Coord. Chem. Rev.* **2017**, *339*, 17−103.
(17) Kumar, P.; SantaLucia, D. J.; Kaniewska-Laskowska, K.; Lindeman, S. V.; Ozarowski, A.; Krzystek, J.; Ozerov, M.; Telser, J.; Berry, J. F.; Fiedler, A. T. Probing the Magnetic Anisotropy of Co(II) Complexes Featuring Redox-Active Ligands. *Inorg. Chem.* **2020**, *59*, 16178−16193.
(18) Boča, R. Zero-field splitting in metal complexes. *Coord. Chem. Rev.* **2004**, *248*, 757−815.
(19) Sun, J. Z.; Safranski, C.; Trouilloud, P.; D'Emic, C.; Hashemi, P.; Hu, G. Stochastic magnetic tunnel junction with easy-plane dominant anisotropy. *Phys. Rev. B* **2023**, *107*, No. 184433.
(20) Schilling, R., In *Quantum Tunneling of Magnetization—QTM'94*, eds. Gunther, L.; Barbara, B., Springer: Dordrecht, 1995; pp 59−76, .
(21) Pilbrow, J. R. Effective *g* values for $S = 3/2$ and $S = 5/2$. *J. Magn. Reson.* **1978**, *31*, 479−490.
(22) Suturina, E. A.; Maganas, D.; Bill, E.; Atanasov, M.; Neese, F. Magneto-Structural Correlations in a Series of Pseudotetrahedral $[Co^{II}(XR)_4]^{2-}$ Single Molecule Magnets: An ab Initio Ligand Field Study. *Inorg. Chem.* **2015**, *54*, 9948−9961.
(23) Rechkemmer, Y.; Breitgoff, F. D.; Van Der Meer, M.; Atanasov, M.; Hakl, M.; Orlita, M.; Neugebauer, P.; Neese, F.; Sarkar, B.; Van Slageren, J. A four-coordinate cobalt(II) single-ion magnet with coercivity and a very high energy barrier. *Nat. Commun.* **2016**, *7*, 10467.
(24) Graham, M. J.; Zadrozny, J. M.; Fataftah, M. S.; Freedman, D. E. Forging Solid-State Qubit Design Principles in a Molecular Furnace. *Chem. Mater.* **2017**, *29*, 1885−1897.
(25) Pedersen, K. S.; Woodruff, D. N.; Singh, S. K.; Tressaud, A.; Durand, E.; Atanasov, M.; Perlepe, P.; Ollefs, K.; Wilhelm, F.; Mathonière, C.; Neese, F.; Rogalev, A.; Bendix, J.; Clérac, R. $[OsF_6]^{x-}$: Molecular Models for Spin-Orbit Entangled Phenomena. *Chem.—Eur. J.* **2017**, *23*, 11244−11248.
(26) Moseley, D. H.; Stavretis, S. E.; Thirunavukkuarasu, K.; Ozerov, M.; Cheng, Y.; Daemen, L. L.; Ludwig, J.; Lu, Z.; Smirnov, D.; Brown, C. M.; Pandey, A.; Ramirez-Cuesta, A. J.; Lamb, A. C.; Atanasov, M.; Bill, E.; Neese, F.; Xue, Z.-L. Spin−phonon couplings in transition metal complexes with slow magnetic relaxation. *Nat. Commun.* **2018**, *9*, 2572.
(27) Stavretis, S. E.; Cheng, Y.; Daemen, L. L.; Brown, C. M.; Moseley, D. H.; Bill, E.; Atanasov, M.; Ramirez-Cuesta, A. J.; Neese, F.; Xue, Z.-L. Probing Magnetic Excitations in CoII Single-Molecule Magnets by Inelastic Neutron Scattering. *Eur. J. Inorg. Chem.* **2019**, *2019*, 1119−1127.
(28) Stavretis, S. E.; Moseley, D. H.; Fei, F.; Cui, H.-H.; Cheng, Y.; Podlesnyak, A. A.; Wang, X.; Daemen, L. L.; Hoffmann, C. M.; Ozerov, M.; Lu, Z.; Thirunavukkuarasu, K.; Smirnov, D.; Chang, T.; Chen, Y.-S.; Ramirez-Cuesta, A. J.; Chen, X.-T.; Xue, Z.-L. Spectroscopic Studies of the Magnetic Excitation and Spin-Phonon Couplings in a Single-Molecule Magnet. *Chem.—Eur. J.* **2019**, *25*, 15846−15857.
(29) Thomsen, M. K.; Nyvang, A.; Walsh, J. P. S.; Bunting, P. C.; Long, J. R.; Neese, F.; Atanasov, M.; Genoni, A.; Overgaard, J. Insights into Single-Molecule-Magnet Behavior from the Experimental Electron Density of Linear Two-Coordinate Iron Complexes. *Inorg. Chem.* **2019**, *58*, 3211−3218.
(30) Moseley, D. H.; Stavretis, S. E.; Zhu, Z.; Guo, M.; Brown, C. M.; Ozerov, M.; Cheng, Y.; Daemen, L. L.; Richardson, R.; Knight, G.; Thirunavukkuarasu, K.; Ramirez-Cuesta, A. J.; Tang, J.; Xue, Z.-L. Inter-Kramers Transitions and Spin−Phonon Couplings in a Lanthanide-Based Single-Molecule Magnet. *Inorg. Chem.* **2020**, *59*, 5218−5230.
(31) Widener, C. N.; Bone, A. N.; Ozerov, M.; Richardson, R.; Lu, Z.; Thirunavukkuarasu, K.; Smirnov, D.; Chen, X.-T.; Xue, Z.-L. Direct Observation of Magnetic Transitions in a Nickel(II) Complex with Large Anisotropy. *Chin. J. Inorg. Chem.* **2020**, *35*, 1149−1156.
(32) Vyaselev, O. M.; Kushch, N. D.; Yagubskii, E. B.; Maximova, O. V.; Vasiliev, A. N. Spin dynamics in two $[ReF_6]$-based single-molecule magnets from NMR and ac susceptibility measurements. *Phys. Rev. B* **2020**, *101*, No. 134427.
(33) Bone, A. N.; Widener, C. N.; Moseley, D. H.; Liu, Z.; Lu, Z.; Cheng, Y.; Daemen, L. L.; Ozerov, M.; Telser, J.; Thirunavukkuarasu, K.; Smirnov, D.; Greer, S. M.; Hill, S.; Krzystek, J.; Holldack, K.; Aliabadi, A.; Schnegg, A.; Dunbar, K. R.; Xue, Z.-L. Applying Unconventional Spectroscopies to the Single-Molecule Magnets $Co(PPh_3)_2X_2$ (X = Cl, Br, I): Unveiling Magnetic Transitions and Spin-Phonon Coupling. *Eur. J. Chem.* **2021**, *27*, 11110−11125.
(34) Moseley, D. H.; Liu, Z.; Bone, A. N.; Stavretis, S. E.; Singh, S. K.; Atanasov, M.; Lu, Z.; Ozerov, M.; Thirunavukkuarasu, K.; Cheng, Y.; Daemen, L. L.; Lubert-Perquel, D.; Smirnov, D.; Neese, F.; Ramirez-Cuesta, A. J.; Hill, S.; Dunbar, K. R.; Xue, Z.-L. Comprehensive Studies of Magnetic Transitions and Spin−Phonon Couplings in the Tetrahedral Cobalt Complex $Co(AsPh_3)_2I_2$. *Inorg. Chem.* **2022**, *61*, 17123−17136.
(35) Tin, P.; Jenkins, M. J.; Xing, J.; Caci, N.; Gai, Z.; Jin, R.; Wessel, S.; Krzystek, J.; Li, C.; Daemen, L. L.; Cheng, Y.; Xue, Z.-L. Haldane topological spin-1 chains in a planar metal-organic framework. *Nat. Commun.* **2023**, *14*, 5454.
(36) Gupta, S. K.; Rao, S. V.; Demeshko, S.; Dechert, S.; Bill, E.; Atanasov, M.; Neese, F.; Meyer, F. Air-stable four-coordinate cobalt(II) single-ion magnets: experimental and ab initio ligand field analyses of correlations between dihedral angles and magnetic anisotropy. *Chem. Sci.* **2023**, *14*, 6355−6374.
(37) Vaidya, S.; Tewary, S.; Singh, S. K.; Langley, S. K.; Murray, K. S.; Lan, Y.; Wernsdorfer, W.; Rajaraman, G.; Shanmugam, M. What Controls the Sign and Magnitude of Magnetic Anisotropy in Tetrahedral Cobalt(II) Single-Ion Magnets? *Inorg. Chem.* **2016**, *55*, 9564−9578.
(38) Fataftah, M. S.; Zadrozny, J. M.; Rogers, D. M.; Freedman, D. E. A Mononuclear Transition Metal Single-Molecule Magnet in a Nuclear Spin-Free Ligand Environment. *Inorg. Chem.* **2014**, *53*, 10716−10721.
(39) Sottini, S.; Poneti, G.; Ciattini, S.; Levesanos, N.; Ferentinos, E.; Krzystek, J.; Sorace, L.; Kyritsis, P. Magnetic Anisotropy of Tetrahedral Co^{II} Single-Ion Magnets: Solid-State Effects. *Inorg. Chem.* **2016**, *55*, 9537−9548.
(40) Cotton, F. A. *Chemical Applications of Group Theory*, 3rd ed., Ch. 9; Wiley, 1990.
(41) Zadrozny, J. M.; Long, J. R. Slow Magnetic Relaxation at Zero Field in the Tetrahedral Complex $[Co(SPh)_4]^{2-}$. *J. Am. Chem. Soc.* **2011**, *133*, 20732−20734.
(42) Idešicová, M.; Dlháň, Ľ.; Moncol', J.; Titiš, J.; Boča, R. Zero-field splitting in tetracoordinate Co(II) complexes. *Polyhedron* **2012**, *36*, 79−84.
(43) Bruno, R.; Vallejo, J.; Marino, N.; De Munno, G.; Krzystek, J.; Cano, J.; Pardo, E.; Armentano, D. Cytosine Nucleobase Ligand: A Suitable Choice for Modulating Magnetic Anisotropy in Tetrahedrally Coordinated Mononuclear Co(II) Compounds. *Inorg. Chem.* **2017**, *56*, 1857−1864.
(44) Chen, S.-Y.; Lv, W.; Cui, H.-H.; Chen, L.; Zhang, Y.-Q.; Chen, X.-T.; Wang, Z.; Ouyang, Z.-W.; Yan, H.; Xue, Z.-L. Magnetic anisotropies and slow magnetic relaxation of three tetrahedral tetrakis(pseudohalido)−cobalt(II) complexes. *New J. Chem.* **2021**, *45*, 16852−16861.

https://doi.org/10.1021/acs.inorgchem.6c00405
Inorg. Chem. 2026, 65, 12818−12834

(45) Korchagin, D. V.; Shilov, G. V.; Aldoshin, S. M.; Morgunov, R. B.; Talantsev, A. D.; Yureva, E. A. Halogen atom effect on the magnetic anisotropy of pseudotetrahedral Co(II) complexes with a quinoline ligand. *Polyhedron* **2015**, *102*, 147−151.
(46) Saber, M. R.; Dunbar, K. R. Ligands effects on the magnetic anisotropy of tetrahedral cobalt complexes. *Chem. Commun.* **2014**, *50*, 12266−12269.
(47) Lv, W.; Cui, H.-H.; Chen, L.; Zhang, Y.-Q.; Chen, X.-T.; Wang, Z.; Ouyang, Z.-W.; Xue, Z.-L. Magnetic anisotropy of two tetrahedral Co(II)-halide complexes with triphenylphosphine ligands. *Dalton Trans.* **2022**, *51*, 7530−7538.
(48) Lim, A. R. Interpretation of the crystal growth, phase transition, and molecular dynamics of $[N(CH_3)_4]_2ZnBr_4$ crystals by replacing partially the Zn^{2+} ions with Co^{2+} ions. *J. Mol. Struct.* **2019**, *1197*, 471−477.
(49) Stucky, G. D.; Folkers, J. B.; Kistenmacher, T. J. The crystal and molecular structure of tetraethylammonium tetrachloronickelate(II). *Acta Crystallogr.* **1967**, *23*, 1064−1070.
(50) Holm, R. H.; Cotton, F. A. Magnetic Investigations of Spin-Free Cobaltous Complexes. I. Tetrahalo Cobalt(II) Ions. *J. Chem. Phys.* **1959**, *31*, 788−792.
(51) McElearney, J. N.; Shankle, G. E.; Schwartz, R. W.; Carlin, R. L. Low-Temperature Magnetic Characteristics of Tetrahedral $CoCl4^{2-}$. II. Nature of the Phase Transition in $[(C_2H_5)_4N]_2CoCl_4$. *J. Chem. Phys.* **1972**, *56*, 3755−3758.
(52) Adams, D. M.; Chatt, J.; Davidson, J. M.; Gerratt, J. The far-infrared spectra (190−460 cm^{-1}) of tetraethylammonium salts of some complex chlorides and bromides. *J. Chem. Soc.* **1963**, *0*, 2189−2194.
(53) Rivoal, J. C.; Briat, B. Magnetic circular dichroism studies of the charge-transfer transitions in tetrachloro and tetrabromocomplexes of transition metal ions. *Mol. Phys.* **1974**, *27*, 1081−1108.
(54) Morosin, B.; Lingafelter, E. C. The crystal structure of tetramethylammonium tetrachlorozincate and tetrachlorocobaltate. *Acta Crystallogr.* **1959**, *12*, 611−612.
(55) Ros, P. The absorption spectra of R_2CoBr_4, R_2NiBr_4 and R_2CuBr_4 [R = $(C_2H_5)_4N$]. *Recl. Trav. Chim. Pay-B* **1963**, *82*, 823−827.
(56) Cotton, F. A.; Goodgame, D. M. L.; Goodgame, M. The electronic structures of tetrahedral cobalt(II) complexes. *J. Am. Chem. Soc.* **1961**, *83*, 4690−4699.
(57) Clark, R. J. H.; Dunn, T. M. The infrared spectra of some tetrahedral inorganic complex halides. *J. Chem. Soc.* **1963**, 1198−1201.
(58) Hamer, N. K. The spectra of some tetrahedral halide complexes of transition metal ions. *Mol. Phys.* **1963**, *6*, 257−264.
(59) Sabatini, A.; Sacconi, L. Far-infrared spectra of some tetrahalo metal complexes. *J. Am. Chem. Soc.* **1964**, *86*, 17−20.
(60) Melia, T. P.; Merrifield, R. Thermal properties of transition-metal compounds. Part V. Heat capacity measurements on $[NMe_4]_2MCl_4$ (M= iron, cobalt, or copper),$[NEt_4]_2CuCl_4$, and Cs_2CoCl_4. *J. Chem. Soc. A* **1971**, 1258−1261.
(61) Gerloch, M.; Lewis, J.; Rickards, R. Magnetic anisotropy and second-order crystal fields in some tetragonally distorted tetrahedral cobalt(II) ions. *J. Chem. Soc., Dalton Trans.* **1972**, 980−986.
(62) Landi, E.; Vacatello, M. New disordered polymorphs in long chain alkylammonium tetrachlorocobaltates (II). *Thermochim. Acta* **1975**, *12*, 141−146.
(63) Jha, N.; Saxena, A. A search for transition in tetrahalocobaltates (II). *Inorg. Chim. Acta* **1977**, *22*, L21−L22.
(64) Jha, N.; Saxena, A. Mixed tetrahalocobaltates (II). *Inorg. Chim. Acta* **1978**, *26*, 201−205.
(65) Laiho, R.; Treshchalov, A. Interaction of the 2E(D) state of Co^{2+} with a jahn-teller active mode in $[N(CH_3)_4]_2CoCl_4$. *Chem. Phys. Lett.* **1981**, *80*, 576−579.
(66) Hasebe, K.; Mashiyama, H.; Tanisaki, S.; Gesi, K. X-ray study of the phase transitions in $[N(CH_3)_4]_2ZnBr_4$ and $[N(CH_3)_4]_2CoBr_4$. *J. Phys. Soc. Jpn.* **1984**, *53*, 1866−1868.
(67) Wei, H. H.; Ho, L. Z. gamma.-Ray-induced linkage isomerization of tetrahedral thiocyanato complexes of iron(II). *Inorg. Chem.* **1984**, *23*, 624−627.
(68) Wolthuis, A.; Huiskamp, W.; De Jongh, L.; Carlin, R. Investigation of structural phase transitions in some $[(C_2H_5)_4N]_2MX_4$ compounds, with M= Co, Zn, Mn, and X= Cl, Br. *Phys. B+C* **1986**, *142*, 301−319.
(69) Hipps, K. W.; Mazur, U. $^4A_2$-$^4T_2$ and $^4A_2$-$^4T_1$ electronic transitions in cobalt(II) tetrachloride: an FT-IR and inelastic electron tunneling spectroscopy study. *J. Am. Chem. Soc.* **1987**, *109*, 3861−3865.
(70) Nishihata, Y.; Sawada, A.; Kasatani, H.; Terauchi, H. Structure of tetramethylammonium tetrabromocobaltate at room temperature. *Acta Crystallogr., C* **1993**, *49*, 1939−1941.
(71) Banerjee, A.; Verma, A.; Roy, S. Alkali metals and $[MCl_4]^{2-}$ structure: tetrahedral structure of Cs_2MCl_4 complexes. *J. Indian Chem. Soc.* **1995**, *72*, 77−79.
(72) Buchhorn, M.; Deeth, R. J.; Krewald, V. Revisiting the Fundamental Nature of Metal-Ligand Bonding: An Impartial and Automated Fitting Procedure for Angular Overlap Model Parameters. *Chem.—Eur. J.* **2022**, *28*, No. e202103775.
(73) Mukda, B. A.; Giantsidis, J.; Landee, C. P.; Dickie, D. A.; Wikaira, J. L.; Turnbull, M. M. Magnetically tunable tetrahedral cobalt(II) halide salts. *J. Coord. Chem.* **2024**, *77*, 2582−2603.
(74) Sen, A.; Roy, S.; Peter, S. C.; Paul, A.; Waghmare, U. V.; Sundaresan, A. Order-disorder structural phase transition and magnetocaloric effect in organic-inorganic halide hybrid $(C_2H_5NH_3)_2CoCl_4$. *J. Solid State Chem.* **2018**, *258*, 431−440.
(75) Piecha-Bisiorek, A.; Bieńko, A.; Jakubas, R.; Boča, R.; Weselski, M.; Kinzhybalo, V.; Pietraszko, A.; Wojciechowska, M.; Medycki, W.; Kruk, D. Physical and Structural Characterization of Imidazolium-Based Organic−Inorganic Hybrid: $(C_3N_2H_5)_2[CoCl_4]$. *J. Phys. Chem. A* **2016**, *120*, 2014−2021.
(76) Carnevale, D. J.; Landee, C. P.; Turnbull, M. M.; Winn, M.; Xiao, F. Co(II) halide complexes with 2-amino-3-methylpyridinium and 2-amino-5-methylpyridinium: synthesis, crystal structures, and magnetic properties. *J. Coord. Chem.* **2010**, *63*, 2223−2238.
(77) Ksiądzyna, M.; Kinzhybalo, V.; Bieńko, A.; Medycki, W.; Jakubas, R.; Rajnák, C.; Boča, R.; Ozarowski, A.; Ozerov, M.; Piecha-Bisiorek, A. Symmetry-breaking phase transitions, dielectric and magnetic properties of pyrrolidinium-tetrahalidocobaltates. *Inorg. Chem. Front.* **2022**, *9*, 2353−2364.
(78) Styczeń, E.; Warnke, Z.; Wyrzykowski, D.; Kłak, J.; Mroziński, J.; Sikorski, A. Bis(tetraethylammonium) tetrabromocobaltate(II) and bis(tetrabutylammonium) tetrabromomanganate(II): structure and magnetic properties. *Struct. Chem.* **2010**, *21*, 269−276.
(79) Kandhaswamy, M. A.; Srinivasan, V. Synthesis and characterization of tetraethylammonium tetrachlorocobaltate crystals. *Bull. Mater. Sci.* **2002**, *25*, 41−45.
(80) Starova, G. L.; Skripkin, M. Y.; Gusev, I. M. Structure of complex bromides crystallizing in MBr_2-NEt_4Br-H_2O systems (M = Cd, Cu, Co) at 25 °C. *Russ. J. Gen. Chem.* **2010**, *80*, 1236−1241.
(81) Rheingold, A. L. D.; Neville, S. Experimental Crystal Structure Determination of $(NEt_4)_2[CoI_4]$. *CSD Commun.* **2016**.
(82) Ozerov, M.; Bernáth, B.; Kamenskyi, D.; Redlich, B.; Van Der Meer, A. F. G.; Christianen, P. C. M.; Engelkamp, H.; Maan, J. C. A THz spectrometer combining the free electron laser FLARE with 33 T magnetic fields. *Appl. Phys. Lett.* **2017**, *110*, No. 094106.
(83) Zvyagin, S. A.; Ozerov, M.; Čižmár, E.; Kamenskyi, D.; Zherlitsyn, S.; Herrmannsdörfer, T.; Wosnitza, J.; Wünsch, R.; Seidel, W. Terahertz-range free-electron laser electron spin resonance spectroscopy: Techniques and applications in high magnetic fields. *Rev. Sci. Instrum.* **2009**, *80*, No. 073102.
(84) Liu, J.-J.; Meng, Y.-S.; Hlavička, I.; Orlita, M.; Jiang, S.-D.; Wang, B.-W.; Gao, S. Determination of zero-field splitting in Co^{2+} halide complexes with magnetic and far-IR measurements. *Dalton Trans.* **2017**, *46*, 7408−7411.

https://doi.org/10.1021/acs.inorgchem.6c00405
Inorg. Chem. 2026, 65, 12818−12834

(85) Bencini, A.; Benelli, C.; Gatteschi, D. The angular overlap model for the description of the paramagnetic properties of transition metal complexes. *Coord. Chem. Rev.* **1984**, *60*, 131−169.
(86) Nover, J. N.; Schmidtke, H.-H. Low Symmetry Ligand Field Splittings in Optical Spectra of Pseudotetrahedral Co(II) Complexes with Halogenide and Chalcogenide Ligands. *Chem. Phys.* **1999**, *241*, 179−191.
(87) Dunsmuir, J. T. R.; Lane, A. P. Far-Infrared Single Crystal Reflectance Spectra of Some Tetra-Alkylammonium Tetrachlorometallates; Influence of Crystal Field Effects and Distortion on the Vibrations of the "Tetrahedral Anions". *J. Chem. Soc. A* **1971**, 2781−2785.
(88) Figgis, B. N.; Lewis, J. The Magnetic Properties of Transition Metal Complexes. *Prog. Inorg. Chem.* **1964**, *6*, 37−239.
(89) Mabbs, F. E.; Machin, D. J. *Magnetism and Transition Metal Complexes, Table 1.3 (p. 21)*, Dover: Mineola, NY, 1973.
(90) Kahn, O.; *Molecular Magnetism*, 1993.
(91) Chilton, N. F.; Anderson, R. P.; Turner, L. D.; Soncini, A.; Murray, K. S. PHI: A powerful new program for the analysis of anisotropic monomeric and exchange-coupled polynuclear d-and f-block complexes. *J. Comput. Chem.* **2013**, *34*, 1164−1175.
(92) Kahn, O.; Larionova, J.; Yakhmi, J. V. Molecular Magnetic Sponges. *Chem.—Eur. J.* **1999**, *5*, 3443−3449.
(93) Krzystek, J.; Telser, J. Measuring giant anisotropy in paramagnetic transition metal complexes with relevance to single-ion magnetism. *Dalton Trans.* **2016**, *45*, 16751−16763.
(94) Hand, A. T.; Watson-Sanders, B. D.; Xue, Z.-L. Spectroscopic techniques to probe magnetic anisotropy and spin-phonon coupling in metal complexes. *Dalton Trans.* **2024**, *53*, 4390−4405.
(95) Krzystek, J.; Ozarowski, A.; Telser, J. Multi-frequency, high-field EPR as a powerful tool to accurately determine zero-field splitting in high-spin transition metal coordination complexes. *Coord. Chem. Rev.* **2006**, *250*, 2308−2324.
(96) Krzystek, J.; Swenson, D. C.; Zvyagin, S. A.; Smirnov, D.; Ozarowski, A.; Telser, J. Cobalt(II) "Scorpionate" Complexes as Models for Cobalt-Substituted Zinc Enzymes: Electronic Structure Investigation by High-Frequency and -Field Electron Paramagnetic Resonance Spectroscopy. *J. Am. Chem. Soc.* **2010**, *132*, 5241−5253.
(97) Nagelski, A. L.; Ozerov, M.; Fataftah, M. S.; Krzystek, J.; Greer, S. M.; Holland, P. L.; Telser, J. Electronic Structure of Three-Coordinate FeII and CoII β-Diketiminate Complexes. *Inorg. Chem.* **2024**, *63*, 4511−4526.
(98) Świtlicka, A.; Machura, B.; Penkala, M.; Bieńko, A.; Bieńko, D. C.; Titiš, J.; Rajnák, C.; Boča, R.; Ozarowski, A.; Ozerov, M. Slow Magnetic Relaxation in Cobalt(II) Field-Induced Single-Ion Magnets with Positive Large Anisotropy. *Inorg. Chem.* **2018**, *57*, 12740−12755.
(99) Choroba, K.; Palion-Gazda, J.; Machura, B.; Bieńko, A.; Wojtala, D.; Bieńko, D.; Rajnák, C.; Boča, R.; Ozarowski, A.; Ozerov, M. Large Magnetic Anisotropy in Mono- and Binuclear cobalt(II) Complexes: The Role of the Distortion of the Coordination Sphere in Validity of the Spin-Hamiltonian Formalism. *Inorg. Chem.* **2024**, *63*, 1068−1082.
(100) Dubroca, T.; Ozarowski, A.; Sunatsuki, Y.; Telser, J.; Hill, S.; Krzystek, J. Benefitting from Magnetic Field-Induced Torquing in Terahertz EPR of a Mn^{III} Coordination Complex. *Appl. Magn. Reson.* **2025**, *56*, 137.
(101) Lv, W.; Chen, L.; Chen, X.-T.; Yan, H.; Wang, Z.; Ouyang, Z.-W.; Xue, Z.-L. Structures and magnetic anisotropies of two seven-coordinate Co(II)−nitrate complexes showing slow magnetic relaxation. *New J. Chem.* **2023**, *47*, 15553−15560.
(102) Cui, H.-H.; Zhang, Y.-Q.; Chen, X.-T.; Wang, Z.; Xue, Z.-L. Magnetic anisotropy and slow magnetic relaxation processes of cobalt(II)-pseudohalide complexes. *Dalton Trans.* **2019**, *48*, 10743−10752.
(103) Chen, S.-Y.; Cui, H.-H.; Zhang, Y.-Q.; Wang, Z.; Ouyang, Z.-W.; Chen, L.; Chen, X.-T.; Yan, H.; Xue, Z.-L. Magnetic anisotropy and relaxation behavior of six-coordinate tris(pivalato)-Co(II) and -Ni(II) complexes. *Dalton Trans.* **2018**, *47*, 10162−10171.
(104) Cui, H.-H.; Ding, M.-M.; Zhang, X.-D.; Lv, W.; Zhang, Y.-Q.; Chen, X.-T.; Wang, Z.; Ouyang, Z.-W.; Xue, Z.-L. Magnetic anisotropy in square pyramidal cobalt(II) complexes supported by a tetraazo macrocyclic ligand. *Dalton Trans.* **2020**, *49*, 14837−14846.
(105) Telser, J. A perspective on applications of ligand-field analysis: inspiration from electron paramagnetic resonance spectroscopy of coordination complexes of transition metal ions. *J. Braz. Chem. Soc.* **2006**, *17*, 1501−1515.
(106) Xue, Z.-L.; Ramirez-Cuesta, A. J.; Brown, C. M.; Calder, S.; Cao, H.; Chakoumakos, B. C.; Daemen, L. L.; Huq, A.; Kolesnikov, A. I.; Mamontov, E.; Podlesnyak, A. A.; Wang, X. Neutron Instruments for Research in Coordination Chemistry. *Eur. JIC* **2019**, *2019*, 1065−1089.
(107) Dunstan, M. A.; Mole, R. A.; Boskovic, C. Inelastic Neutron Scattering of Lanthanoid Complexes and Single-Molecule Magnets. *Eur. J. Inorg. Chem.* **2019**, *2019*, 1090−1105.
(108) Colacio, E.; Ruiz, J.; Ruiz, E.; Cremades, E.; Krzystek, J.; Carretta, S.; Cano, J.; Guidi, T.; Wernsdorfer, W.; Brechin, E. K. Slow Magnetic Relaxation in a Co^{II}−Y^{III} Single-Ion Magnet with Positive Axial Zero-Field Splitting. *Angew. Chem. In. Ed.* **2013**, *52*, 9130−9134.
(109) Pedersen, K. S.; Ungur, L.; Sigrist, M.; Sundt, A.; Schau-Magnussen, M.; Vieru, V.; Mutka, H.; Rols, S.; Weihe, H.; Waldmann, O.; Chibotaru, L. F.; Bendix, J.; Dreiser, J. Modifying the Properties of 4f Single-Ion Magnets by Peripheral Ligand Functionalisation. *Chem. Sci.* **2014**, *5*, 1650−1660.
(110) Feng, X.; Liu, J.-L.; Pedersen, K. S.; Nehrkorn, J.; Schnegg, A.; Holldack, K.; Bendix, J.; Sigrist, M.; Mutka, H.; Samohvalov, D.; Aguilà, D.; Tong, M.-L.; Long, J. R.; Clérac, R. Multifaceted magnetization dynamics in the mononuclear complex $[Re^{IV}Cl_4(CN)_2]^{2-}$. *Chem. Commun.* **2016**, *52*, 12905−12908.
(111) Sørensen, M. A.; Hansen, U. B.; Perfetti, M.; Pedersen, K. S.; Bartolomé, E.; Simeoni, G. G.; Mutka, H.; Rols, S.; Jeong, M.; Zivkovic, I.; Retuerto, M.; Arauzo, A.; Bartolomé, J.; Piligkos, S.; Weihe, H.; Doerrer, L. H.; van Slageren, J.; Rønnow, H. M.; Lefmann, K.; Bendix, J. Chemical tunnel-splitting-engineering in a dysprosium-based molecular nanomagnet. *Nat. Commun.* **2018**, *9*, 1292.
(112) Perfetti, M.; Sørensen, M. A.; Hansen, U. B.; Bamberger, H.; Lenz, S.; Hallmen, P. P.; Fennell, T.; Simeoni, G. G.; Arauzo, A.; Bartolomé, J.; Bartolomé, E.; Lefmann, K.; Weihe, H.; van Slageren, J.; Bendix, J. Magnetic Anisotropy Switch: Easy Axis to Easy Plane Conversion and Vice Versa. *Adv. Funct. Mater.* **2018**, *28*, No. 1801846.
(113) Bonde, N. A.; Appel, M.; Ollivier, J.; Weihe, H.; Bendix, J. Unequal sensitivities of energy levels in a high-symmetry Ho^{3+} complex towards lattice distortions. *Chem. Commun.* **2022**, *58*, 7431−7434.
(114) Vonci, M.; Giansiracusa, M. J.; Van den Heuvel, W.; Gable, R. W.; Moubaraki, B.; Murray, K. S.; Yu, D.; Mole, R. A.; Soncini, A.; Boskovic, C. Magnetic Excitations in Polyoxotungstate-Supported Lanthanoid Single-Molecule Magnets: An Inelastic Neutron Scattering and ab Initio Study. *Inorg. Chem.* **2017**, *56*, 378−394.
(115) Vonci, M.; Giansiracusa, M. J.; Gable, R. W.; Van den Heuvel, W.; Latham, K.; Moubaraki, B.; Murray, K. S.; Yu, D.; Mole, R. A.; Soncini, A.; Boskovic, C. Ab initio calculations as a quantitative tool in the inelastic neutron scattering study of a single-molecule magnet analogue. *Chem. Commun.* **2016**, *52*, 2091−2094.
(116) Bonde, N. A.; Petersen, J. B.; Sørensen, M. A.; Nielsen, U. G.; Fåk, B.; Rols, S.; Ollivier, J.; Weihe, H.; Bendix, J.; Perfetti, M. Importance of Axial Symmetry in Elucidating Lanthanide−Transition Metal Interactions. *Inorg. Chem.* **2020**, *59*, 235−243.
(117) Hunter, S. C.; Podlesnyak, A. A.; Xue, Z.-L. Magnetic excitations in metalloporphyrins by Inelastic Neutron Scattering: Determination of zero-field splittings in iron, manganese, and chromium complexes. *Inorg. Chem.* **2014**, *53*, 1955−1961.
(118) Fakolujo, A. A.; Bone, A. N.; Smith, B. A.; Song, L.; Cheng, Y.; Daemen, L. L.; Podlesnyak, A. A.; Xue, Z.-L. Magnetic and Phonon Excitations in Iron(III) Porphyrin Complexes Probed by Inelastic Neutron Scattering: Impact of the Perdeuteration of the Porphyrin Ligand. *Inorg. Chem.* **2025**, *64*, 17142−17155.

https://doi.org/10.1021/acs.inorgchem.6c00405
Inorg. Chem. 2026, 65, 12818−12834

(119) Stavretis, S. E.; Atanasov, M.; Podlesnyak, A. A.; Hunter, S. C.; Neese, F.; Xue, Z.-L. Magnetic Transitions in Iron Porphyrin Halides by Inelastic Neutron Scattering and Ab Initio Studies of Zero-Field Splittings. *Inorg. Chem.* **2015**, *54*, 9790−9801.
(120) Chen, L.; Cui, H.-H.; Stavretis, S. E.; Hunter, S. C.; Zhang, Y.-Q.; Chen, X.-T.; Sun, Y.-C.; Wang, Z.; Song, Y.; Podlesnyak, A. A.; Ouyang, Z.-W.; Xue, Z.-L. Slow Magnetic Relaxations in Cobalt(II) Tetranitrate Complexes. Studies of Magnetic Anisotropy by Inelastic Neutron Scattering and High-Frequency and High-Field EPR Spectroscopy. *Inorg. Chem.* **2016**, *55*, 12603−12617.
(121) Pavel, E. G.; Kitajima, N.; Solomon, E. I. Magnetic Circular Dichroism Spectroscopic Studies of Mononuclear Non-Heme Ferrous Model Complexes. Correlation of Excited- and Ground-State Electronic Structure with Geometry. *J. Am. Chem. Soc.* **1998**, *120*, 3949−3962.
(122) Neese, F.; Wennmohs, F.; Becker, U.; Riplinger, C., The ORCA quantum chemistry program package. *J. Chem. Phys.* **2020**, *152*. .
(123) Vassilyeva, O. Y.; Buvaylo, E. A.; Kokozay, V. N.; Skelton, B. W.; Rajnák, C.; Titiš, J.; Boča, R. Long magnetic relaxation time of tetracoordinate Co^{2+} in imidazo[1,5-*a*]pyridinium-based $(C_{13}H_{12}N_3)_2[CoCl_4]$ hybrid salt and $[Co(C_{13}H_{12}N_3)Cl_3]$ molecular complex. *Dalton Trans.* **2019**, *48*, 11278−11284.
(124) Bendix, J., In *Comprehensive Coordination Chemistry II, Vol. 2: Fundamentals: Physical Methods, Theoretical Analysis, and Case Studies*, ed. Lever, A. B. P., Elsevier: Amsterdam, 2003, Vol. *2*, pp 673−676.
(125) Telser, J., DDN software is available at https://edmond.mpg.de/dataset.xhtml?persistentId=doi:10.17617/3.XNQCUE, labeled as "Josh_Telser_sfotware.zip", (accessed Apr. 6, 2026).
(126) van Stapele, R. P.; Beljers, H. G.; Bongers, P. F.; Zijlstra, H. Ground State of Divalent Co Ions in Cs_3CoCl_5 and Cs_3CoBr_5. *J. Chem. Phys.* **1966**, *44*, 3719−3725.
(127) Bendix, J.; Brorson, M.; Schaffer, C. E. Accurate empirical spin-orbit coupling parameters ζ_{nd} for gaseous nd^q transition metal ions. The parametrical multiplet term model. *Inorg. Chem.* **1993**, *32*, 2838−2849.
(128) Brorson, M.; Schäffer, C. E. Orthonormal interelectronic repulsion operators in the parametrical d^q model. Application of the model to gaseous ions. *Inorg. Chem.* **1988**, *27*, 2522−2530.
(129) Miessler, G. L.; Fischer, P. J.; Tarr, D. A. *Inorganic Chemmistry, 5th Ed., Ch. 10, Section 10.4, pp. 382−393*, 5th ed., Pearson: Boston, MA, 2014.
(130) Yang, F.; Zhou, Q.; Zhang, Y.; Zeng, G.; Li, G.; Shi, Z.; Wang, B.; Feng, S. Inspiration from Old Molecules: Field-Induced Slow Magnetic Relaxation in Three Air-Stable Tetrahedral Cobalt(II) Compounds. *Chem. Commun.* **2013**, *49*, 5289.
(131) Reta, D.; Chilton, N. F. Uncertainty estimates for magnetic relaxation times and magnetic relaxation parameters. *Phys. Chem. Chem. Phys.* **2019**, *21*, 23567−23575.
(132) Blackmore, W. J. A.; Gransbury, G. K.; Evans, P.; Kragskow, J. G. C.; Mills, D. P.; Chilton, N. F. Characterisation of magnetic relaxation on extremely long timescales. *Phys. Chem. Chem. Phys.* **2023**, *25*, 16735−16744.
(133) IUCr, International Tables for Crystallography, Space group 18 ($P2_12_12$), https://it.iucr.org/Ac/ch2o3v0001/sgtable2o3o018/, (accessed Apr. 6, 2026).
(134) IUCr, International Tables for Crystallography, Space group 137 ($P4_2/nmc$), https://it.iucr.org/Ac/ch2o3v0001/sgtable2o3o137/).
(135) Bunting, P. C.; Atanasov, M.; Damgaard-Møller, E.; Perfetti, M.; Crassee, I.; Orlita, M.; Overgaard, J.; van Slageren, J.; Neese, F.; Long, J. R. A linear cobalt(II) complex with maximal orbital angular momentum from a non-Aufbau ground state. *Science* **2018**, *362*, No. eaat7319.
(136) Bone, A. N.; Stavretis, S. E.; Krzystek, J.; Liu, Z.; Chen, Q.; Gai, Z.; Wang, X.; Steren, C. A.; Powers, X. B.; Podlesnyak, A. A.; Chen, X.-T.; Telser, J.; Zhou, H.; Xue, Z.-L. Manganese tetraphenylporphyrin bromide and iodide. Studies of structures and magnetic properties. *Polyhedron* **2020**, *184*, No. 114488.
(137) Tin, P.; Stavretis, S. E.; Ozerov, M.; Krzystek, J.; Ponomaryov, A. N.; Zvyagin, S. A.; Wosnitza, J.; Chen, C.-C.; Chen, P. P. Y.; Telser, J.; Xue, Z.-L. Advanced Magnetic Resonance Studies of Tetraphenylporphyrinatoiron(III) Halides. *Appl. Magn. Reson.* **2020**, *51*, 1411−1432.
(138) Viciano-Chumillas, M.; Blondin, G.; Clémancey, M.; Krzystek, J.; Ozerov, M.; Armentano, D.; Schnegg, A.; Lohmiller, T.; Telser, J.; Lloret, F.; Cano, J. Single-Ion Magnetic Behaviour in an Iron(III) Porphyrin Complex: A Dichotomy Between High Spin and 5/2−3/2 Spin Admixture. *Chem.—Eur. J.* **2020**, *26*, 14242−14251.
(139) Hughey, K. D.; Harms, N. C.; O'Neal, K. R.; Clune, A. J.; Monroe, J. C.; Blockmon, A. L.; Landee, C. P.; Liu, Z.; Ozerov, M.; Musfeldt, J. L. Spin−Lattice Coupling Across the Magnetic Quantum-Phase Transition in Copper-Containing Coordination Polymers. *Inorg. Chem.* **2020**, *59*, 2127−2135.
(140) Vallejo, J.; Viciano-Chumillas, M.; Lloret, F.; Julve, M.; Castro, I.; Krzystek, J.; Ozerov, M.; Armentano, D.; De Munno, G.; Cano, J. Coligand Effects on the Field-Induced Double Slow Magnetic Relaxation in Six-Coordinate Cobalt(II) Single-Ion Magnets (SIMs) with Positive Magnetic Anisotropy. *Inorg. Chem.* **2019**, *58*, 15726−15740.
(141) Devkota, L.; SantaLucia, D. J.; Wheaton, A. M.; Pienkos, A. J.; Lindeman, S. V.; Krzystek, J.; Ozerov, M.; Berry, J. F.; Telser, J.; Fiedler, A. T. Spectroscopic and Magnetic Studies of Co(II) Scorpionate Complexes: Is There a Halide Effect on Magnetic Anisotropy? *Inorg. Chem.* **2023**, *62*, 5984−6002.
(142) Ferentinos, E.; Tzeli, D.; Sottini, S.; Groenen, E. J. J.; Ozerov, M.; Poneti, G.; Kaniewska-Laskowska, K.; Krzystek, J.; Kyritsis, P. Magnetic anisotropy and structural flexibility in the field-induced single ion magnets $[Co\{(OPPh_2)(EPPh_2)N\}_2]$, E = S, Se, explored by experimental and computational methods. *Dalton Trans.* **2023**, *52*, 2036−2050.
(143) Landart-Gereka, A.; Quesada-Moreno, M. M.; Palacios, M. A.; Díaz-Ortega, I. F.; Nojiri, H.; Ozerov, M.; Krzystek, J.; Colacio, E. Pushing up the easy-axis magnetic anisotropy and relaxation times in trigonal prismatic Co^{II} mononuclear SMMs by molecular structure design. *Chem. Commun.* **2023**, *59*, 952−955.
(144) Kragskow, J. G. C.; Marbey, J.; Buch, C. D.; Nehrkorn, J.; Ozerov, M.; Piligkos, S.; Hill, S.; Chilton, N. F. Analysis of vibronic coupling in a 4f molecular magnet with FIRMS. *Nat. Commun.* **2022**, *13*, 825.
(145) Perfetti, M.; Gysler, M.; Rechkemmer-Patalen, Y.; Zhang, P.; Taştan, H.; Fischer, F.; Netz, J.; Frey, W.; Zimmermann, L. W.; Schleid, T.; Hakl, M.; Orlita, M.; Ungur, L.; Chibotaru, L.; Brock-Nannestad, T.; Piligkos, S.; van Slageren, J. Determination of the electronic structure of a dinuclear dysprosium single molecule magnet without symmetry idealization. *Chem. Sci.* **2019**, *10*, 2101−2110.
(146) Hand, A. T.; Fakolujo, A. A.; Krzystek, J.; Ozerov, M.; Daemen, L. L.; Xing, J.; Gai, Z.; Jin, R.; Telser, J.; Podlesnyak, A. A.; Xue, Z.-L. Advanced spectroscopic studies of $(PPh_4)_2[Co(N_3)_4]$, a field-induced single-ion magnet. *New J. Chem.* **2025**, *49*, 17084−17098.
(147) Jenkins, M. J.; Ozerov, M.; Krzystek, J.; Daemen, L. L.; Cheng, Y.; Xue, Z.-L. Probing magnetic and vibrational properties of trigonal-bipyramidal Co(II) and Ni(II) complexes using advanced spectroscopies. *New J. Chem.* **2025**, *49*, 5740−5756.
(148) Hu, Z.-B.; Gui, L.-A.; Li, L.-H.; Xiao, T.-T.; Hand, A. T.; Tin, P.; Ozerov, M.; Peng, Y.; Ouyang, Z.; Wang, Z.; Xue, Z.-L.; Song, Y. Co^{II} single-ion magnet and its multi-dimensional aggregations: Influence of the structural rigidity on magnetic relaxation process. *Chin. Chem. Lett.* **2025**, *36*, No. 109600.
(149) Brackett, G. C.; Richards, P. L.; Caughey, W. S. Far-Infrared Magnetic Resonance in Fe(III) and Mn(III) Porphyrins, Myoglobin, Hemoglobin, Ferrichrome A, and Fe(III) Dithiocarbamates. *J. Chem. Phys.* **1971**, *54*, 4383−4401.
(150) Togo, A.; VASP-DFPT & Phonopy Calculation https://phonopy.github.io/phonopy/vasp-dfpt.html.

https://doi.org/10.1021/acs.inorgchem.6c00405
Inorg. Chem. 2026, 65, 12818−12834

(151) Gill, N. S.; Taylor, F. B.; Hatfield, W. E.; Parker, W. E.; Fountain, C. S.; Bunger, F. L. *Tetrahalo Complexes of Dipositive Metals in the First Transition Series*; Wiley, 1967.
(152) *SAINT, version 6.45, Bruker Analytical X-ray Systems*, Madison, WI, 2003.
(153) Sheldrick, G. M. *SADABS Program for Absorption Correction, version 2.10, Analytical X-ray Systems*, Madison, WI, 2003.
(154) Dolomanov, O. V.; Bourhis, L. J.; Gildea, R. J.; Howard, J. A. K.; Puschmann, H. OLEX2: a complete structure solution, refinement and analysis program. *J. Appl. Crystallogr.* **2009**, *42*, 339−341.
(155) Sheldrick, G. SHELXT - Integrated space-group and crystal-structure determination. *Acta Crystallogr.* **2015**, *A71*, 3−8.
(156) Bourhis, L. J.; Dolomanov, O. V.; Gildea, R. J.; Howard, J. A. K.; Puschmann, H. The anatomy of a comprehensive constrained, restrained refinement program for the modern computing environment - Olex2 dissected. *Acta Crystallogr.* **2015**, *A71*, 59−75.
(157) Bain, G. A.; Berry, J. F. Diamagnetic Corrections and Pascal's Constants. *J. Chem. Educ.* **2008**, *85*, 532−536.
(158) Hassan, A. K.; Pardi, L. A.; Krzystek, J.; Sienkiewicz, A.; Goy, P.; Rohrer, M.; Brunel, L. C. Ultrawide Band Multifrequency High-Field EMR Technique: A Methodology for Increasing Spectroscopic Information. *J. Magn. Reson.* **2000**, *142*, 300−312.
(159) Neese, F. Software update: The ORCA program system—Version 5.0. *WIREs Comput. Mol. Sci.* **2022**, *12*, No. e1606.
(160) Neese, F.; Wennmohs, F.; Hansen, A.; Becker, U. Efficient, approximate and parallel Hartree−Fock and hybrid DFT calculations. A 'chain-of-spheres' algorithm for the Hartree−Fock exchange. *Chem. Phys.* **2009**, *356*, 98−109.
(161) Weigend, F. Accurate Coulomb-fitting basis sets for H to Rn. *Phys. Chem. Chem. Phys.* **2006**, *8*, 1057−1065.
(162) Angeli, C.; Cimiraglia, R.; Evangelisti, S.; Leininger, T.; Malrieu, J.-P. Introduction of n-electron valence states for multi-reference perturbation theory. *J. Chem. Phys.* **2001**, *114*, 10252−10264.
(163) Kresse, G.; Furthmüller, J. Efficient iterative schemes for ab initio total-energy calculations using a plane-wave basis set. *Phys. Rev. B* **1996**, *54*, 11169−11186.
(164) Blöchl, P. E. Projector augmented-wave method. *Phys. Rev. B* **1994**, *50*, 17953−17979.
(165) Kresse, G.; Joubert, D. From ultrasoft pseudopotentials to the projector augmented-wave method. *Phys. Rev. B* **1999**, *59*, 1758−1775.
(166) Perdew, J. P.; Burke, K.; Ernzerhof, M. Generalized Gradient Approximation Made Simple. *Phys. Rev. Lett.* **1996**, *77*, 3865−3868.
(167) Klimeš, J.; Bowler, D. R.; Michaelides, A. Chemical accuracy for the van der Waals density functional. *J. Phys.: Condens. Matter* **2010**, *22*, No. 022201.
(168) Wang, L.; Maxisch, T.; Ceder, G. Oxidation energies of transition metal oxides within the GGA+U framework. *Phys. Rev. B* **2006**, *73*, No. 195107.
(169) Togo, A.; Tanaka, I. First principles phonon calculations in materials science. *Scr. Mater.* **2015**, *108*, 1−5.
(170) Cheng, Y. Q.; Daemen, L. L.; Kolesnikov, A. I.; Ramirez-Cuesta, A. J. Simulation of Inelastic Neutron Scattering Spectra Using OCLIMAX. *J. Chem. Theory Comput.* **2019**, *15*, 1974−1982.

https://doi.org/10.1021/acs.inorgchem.6c00405
Inorg. Chem. 2026, 65, 12818−12834